

AD-A234 858

1

1. DOCUMENTATION PAGE				Form Approved OMB No. 0704-0188	
1a. REPORT SECURITY CLASSIFICATION		1b. RESTRICTIVE MARKINGS			
2a. SECURITY CLASSIFICATION AUTHORITY		3. DISTRIBUTION/AVAILABILITY OF REPORT Approved for public release; Distribution unlimited			
2b. DECLASSIFICATION/DOWNGRADING SCHEDULE					
4. PERFORMING ORGANIZATION REPORT NUMBER(S) PL-TR-91-2066		5. MONITORING ORGANIZATION REPORT NUMBER(S)			
6a. NAME OF PERFORMING ORGANIZATION Phillips Lab, Geophysics Directorate		6b. OFFICE SYMBOL (if applicable) LIS		7a. NAME OF MONITORING ORGANIZATION DTIC ELECTE APR 10 1991 S G D	
6c. ADDRESS (City, State, and ZIP Code) Hanscom AFB Massachusetts 01731-5000		7b. ADDRESS (City, State, and ZIP Code)			
8a. NAME OF FUNDING/SPONSORING ORGANIZATION		8b. OFFICE SYMBOL (if applicable)		9. PROCUREMENT INSTRUMENT IDENTIFICATION NUMBER	
8c. ADDRESS (City, State, and ZIP Code)		10. SOURCE OF FUNDING NUMBERS			
		PROGRAM ELEMENT NO. 61102F		PROJECT NO. 2310 TASK NO. G9 WORK UNIT ACCESSION NO. 03	
11. TITLE (Include Security Classification) The Electrodynamic, Thermal, and Energetic Character of Intense Sun-Aligned Arcs in the Polar Cap					
12. PERSONAL AUTHOR(S) C.E. Valladares*, H.C. Carlson, Jr.					
13a. TYPE OF REPORT Reprint		13b. TIME COVERED FROM _____ TO _____		14. DATE OF REPORT (Year, Month, Day) 1991 April 2	
15. PAGE COUNT 22					
16. SUPPLEMENTARY NOTATION *Institute for Space Research, Boston College, Newton Center, MA- Reprinted from Journal of Geophysical Research, Vol. 96, No. A2, pages 1379-1400, February 1, 1991					
17. COSATI CODES					
FIELD		GROUP		SUB-GROUP	
18. SUBJECT TERMS (Continue on reverse if necessary and identify by block number) Sun-Aligned Arcs, Electrodynamics, Thermal balance					
19. ABSTRACT (Continue on reverse if necessary and identify by block number) <p>The electrodynamic, thermal, and energetic character of stable Sun-aligned arcs in the polar cap can be meaningfully diagnosed by an incoherent scatter radar, provided a suitable observing scheme is selected. We report here such measurements of two intense Sun-aligned arcs. The two arcs were diagnosed on two different nights (February 26 and March 1, 1987) using the Sondre Stromford radar as a stand-alone diagnostic. Repeatable patterns are found in mesoscale area (order <math>10^3</math> km by <math>10^3</math> km) strips of altitude profiles for observed electron and ion gas number densities, temperatures, and line-of-sight velocities, and projected mesoscale area maps of derived electric fields, Pedersen and Hall conductivity, <math>\Sigma_P</math>, <math>\Sigma_H</math>, <math>T_e</math>, <math>T_i</math>, <math>V_e</math>, <math>V_i</math>, <math>\Sigma_P</math>, <math>\Sigma_H</math>, horizontal and field-aligned currents, joule heating rate, and Poynting flux. We confirm, for the first time with continuous mesoscale area maps, that the arcs have the anticipated simple arc electrodynamics. That is, the visual and enhanced ionization signatures of the arc are produced by incoming energetic electrons carrying the outgoing current from the electric field convergence in the arc. Strong electron temperature enhancements (<math>&gt;2000</math> K) are found as expected within the sheets of ionizing particle precipitation. Dawn to dusk decreases in the</p> <p style="text-align: right;">(Cont'd)</p>					
20. DISTRIBUTION/AVAILABILITY OF ABSTRACT <input type="checkbox"/> UNCLASSIFIED/DUNLIMITED <input checked="" type="checkbox"/> SAME AS RPT. <input type="checkbox"/> DTIC USERS		21. ABSTRACT SECURITY CLASSIFICATION Unclassified			
22a. NAME OF RESPONSIBLE INDIVIDUAL H.C. Carlson		22b. TELEPHONE (include Area Code) (617) 377-2860		22c. OFFICE SYMBOL L.I.	

DD Form 1473, JUN 86

Previous editions are obsolete.

SECURITY CLASSIFICATION OF THIS PAGE  
Unclassified

DTIC FILE COPY

BEST  
AVAILABLE COPY

Cont of Block 19:

antisunward plasma flow of order  $1 \text{ km s}^{-1}$ , across order 100 km, correspond to peak electron densities of order  $10^5 \text{ cm}^{-3}$  down to altitudes as low as 120 km, and upward currents of order  $1 \mu\text{A m}^{-2}$ . These data also lead to important implications for the physics of polar cap arcs. The high-velocity (antisunward flow on the dawnside) edge of the arc marks the location of strong persistent Joule heating driven by downward Poynting flux. There is a channel of strongly enhanced ion temperature (well above the electron temperature) along the high-velocity edge of the arc, quantitatively accounted for by ion frictional heating as the strong electric field drags the ions through the neutral gas. The deposition rate into the atmosphere of the net electromagnetic energy well exceeds the net particle energy deposited by the ionizing energetic electron flux. This heating is a substantial source of heat into the polar thermosphere. As estimated by heat into the ions, heat lost by the ions to the neutrals, or energy available from the Poynting and energetic particle flux, several  $\text{ergs cm}^{-2} \text{ s}^{-1}$  are deposited in channels of order 100 km for good fractions of an hour in these arcs; this contributes to resolving the problem of the missing polar thermosphere heat source. Finally, a reasonably simple yet self-consistent, accurate, and comprehensive representation of stable intense Sun-aligned arcs is presented, including the electrodynamic, thermal, and energetic character.

Accession For	
NTIS CRA&I	<input checked="" type="checkbox"/>
DTIC TAB	<input type="checkbox"/>
Unannounced	<input type="checkbox"/>
Justification	
By	
Distribution	
Availability Codes	
Dist	Avail and/or Special
A-1	20

\*Original contains color plates. All DTIC reproductions will be in black and white.

# The Electrodynamic, Thermal, and Energetic Character of Intense Sun-Aligned Arcs in the Polar Cap

C. E. VALLADARES

*Institute for Space Research, Boston College, Newton Center, Massachusetts*

H. C. CARLSON, JR.

*Geophysics Laboratory, Hanscom Air Force Base, Massachusetts*

The electrodynamic, thermal, and energetic character of stable Sun-aligned arcs in the polar cap can be meaningfully diagnosed by an incoherent scatter radar, provided a suitable observing scheme is selected. We report here such measurements of two intense Sun-aligned arcs. The two arcs were diagnosed on two different nights (February 26 and March 1, 1987) using the Sondre Stromfjord radar as a stand-alone diagnostic. Repeatable patterns are found in mesoscale area (order  $10^3$  km by  $10^3$  km) maps of altitude profiles for observed electron and ion gas number densities, temperatures, and line-of-sight velocities, and projected mesoscale area maps of derived electric fields, Pedersen and Hall conductivities ( $N_e$ ,  $T_e$ ,  $T_i$ ,  $V$ ,  $E$ ,  $\Sigma_P$ ,  $\Sigma_H$ ), horizontal and field-aligned currents, joule heating rate, and Poynting flux. We confirm, for the first time with continuous mesoscale area maps, that the arcs have the anticipated simple arc electrodynamics. That is, the visual and enhanced ionization signatures of the arc are produced by incoming energetic electrons carrying the outgoing current from the electric field convergence in the arc. Strong electron temperature enhancements ( $>2000$  K) are found as expected within the sheets of ionizing particle precipitation. Dawn to dusk decreases in the antisunward plasma flow of order  $1 \text{ km s}^{-1}$ , across order 100 km, correspond to peak electron densities of order  $10^5 \text{ cm}^{-3}$  down to altitudes as low as 120 km, and upward currents of order  $1 \mu\text{A m}^{-2}$ . These data also lead to important implications for the physics of polar cap arcs. The high-velocity (antisunward flow on the dawnside) edge of the arc marks the location of strong persistent Joule heating driven by downward Poynting flux. There is a channel of strongly enhanced ion temperature (well above the electron temperature) along the high-velocity edge of the arc, quantitatively accounted for by ion frictional heating as the strong electric field drags the ions through the neutral gas. The deposition rate into the atmosphere of the net electromagnetic energy well exceeds the net particle energy deposited by the ionizing energetic electron flux. This heating is a substantial source of heat into the polar thermosphere. As estimated by heat into the ions, heat lost by the ions to the neutrals, or energy available from the Poynting and energetic particle flux, several  $\text{ergs cm}^{-2} \text{ s}^{-1}$  are deposited in channels of order 100 km for good fractions of an hour in these arcs; this contributes to resolving the problem of the missing polar thermosphere heat source. Finally, a reasonably simple yet self-consistent, accurate, and comprehensive representation of stable intense Sun-aligned arcs is presented, including the electrodynamic, thermal, and energetic character.

## 1. INTRODUCTION

Morphological studies of intense polar cap aurora began during the International Geophysical Year (IGY). Measurements performed during this year at Antarctica [Weill, 1958; Denholm and Bond, 1961] and at Resolute Bay, Canada [Davis, 1960] found intense polar cap arcs oriented in the Sun-Earth direction. Later, a scanning photometer on board ISIS 2 [Berkey et al., 1976; Ismail et al., 1977] and all-sky cameras in Greenland [Lassen and Danielsen, 1978] revealed that the occurrence of intense polar arcs throughout the polar cap correlates well with northward interplanetary magnetic field (IMF).

New initiatives to observe the intense Sun-Earth aligned arcs involved airborne observatories [Romick and Brown, 1971; Eather and Akasofu, 1969] and also particle and optical emission detectors on Defense Meteorological Satellite Program (DMSP) satellites [Meng and Akasofu, 1976; Akasofu, 1976]. The new instrumentation served to indicate that the

polar arcs are usually produced by soft ( $<1$  keV) electrons and to characterize the different types, locations and shapes of intense polar cap auroras.

Statistical and case studies of auroras and particle precipitation in the polar cap indicated that intense polar cap auroras preferentially occur in the morning sector [Gussenhoven, 1982]. The average energy of intense electron precipitation in the polar cap was found to be between 50 and 300 eV [Hardy, 1984]. Burke et al. [1982] inferred that intense polar cap arcs are the optical signature of upward Birkeland currents associated with corresponding velocity gradients.

The DE 1 spacecraft provided images of intense Sun-aligned arcs extending across the polar cap. The transpolar auroras together with the auroral oval resembled the Greek letter theta [Frank et al., 1982, 1986]. The salient features of this striking auroral pattern are the presence of precipitating ions accompanying the energetic electrons ( $>1$  keV), its location in a region of sunward convection, and the possible existence of four cells of plasma convection. Burke et al. [1979] have also presented data suggesting four convecting cells. A valuable description of the convection for different values of the three components of the IMF has been presented by Reiff and Burch [1985]. Their analysis implies a

Copyright 1991 by the American Geophysical Union.

Paper number 90JA01765.  
0148-0227/91/90JA-0176\$05.00

four-cell convection pattern for strong northward IMF and a three-cell convection for smaller positive values of  $B_z$ .

There is a general consensus that some of the intense polar cap Sun-aligned (S-A) arcs are formed in a region of closed field lines [Akasofu *et al.*, 1984; Frank *et al.*, 1986] with precipitating electrons having the characteristics of plasma sheet or plasma sheet boundary layer electrons [Peterson and Shelley, 1984; Obara *et al.*, 1988]. Kan and Burke [1985] have argued that the less intense polar arcs possibly occur on open field lines. Other high-latitude arcs may well correspond to a poleward widened auroral oval [Meng, 1981; Murphree *et al.*, 1982]. Data presented by Huang *et al.* [1987] collected by ISEE 1 during excursions in the magnetotail suggest filaments of plasma sheet plasma extend into the lobes. Even though the filaments have been observed for any orientation of  $B_z$ , their presence reflects the discrete nature of the plasma source and suggests a causal link between the IMF and the formation of the polar cap arcs.

With the advent of intensified imaging photometers, much more common weak stable Sun-aligned arcs were found in the polar cap [Weber and Buchau, 1981]. The Sondrestrom incoherent scatter radar was also used to study the morphology of these weak S-A arcs. Carlson *et al.* [1984] determined sheared (antisunward to sunward reversal) flow which was coincident with bottomside  $F$  region density enhancements and with optical emissions, both produced by the precipitating particles. The plasma velocity gradients coincided with a simple arc electrodynamics interpretation. Robinson *et al.* [1987] obtained the field-aligned currents for a Sun-aligned arc observed near local midnight and merging into the auroral oval. Their measurements implied an upward current on the western edge of the arc and a downward current on the eastern side. Mende *et al.* [1988] have also presented measurements from Sondrestrom. Their observations of multiple polar cap arcs showed a preferential antisunward flow within the arcs.

Carlson *et al.* [1988] have presented convection patterns representing northward  $B_z$  conditions which were obtained by combining the optical emissions associated with S-A arcs and the one-dimensional velocity measurements of DE 2. These quantitatively confirm electron impact production of the arc, and local simple electrodynamics for the arc. Weber *et al.* [1989] used data from a rocket that traversed a polar cap arc to model the circuit parameters of the arc. They also showed enhanced electron temperature variation across the arc.

The purpose of this paper is to examine more comprehensive diagnostics and analysis of the electrodynamics, the energy, and the thermal properties of a few Sun-aligned arcs which were located in the polar cap. The data are more comprehensive by virtue of time continuous measurement, over a wide spatial area, of a significantly more complete set of geophysical parameters. The arcs to be described in this work were probed with the Sondrestrom radar on the evenings of February 26 and March 1, 1987. The common signature of these arcs consists in that they were produced by electrons with energies larger than 1 keV, as deduced from the altitude of significant  $E$  region ionization. Although we diagnosed over 30 stable Sun-aligned arcs, using all-sky imaging photometers (ASIPs) and/or the incoherent scatter radar (ISR) during this campaign, here we will concentrate on only two of these arcs. The arcs we concentrate on are the two most intense, for optimum signal to noise ratio or

measurement statistics on derived parameters. The arc of February 26 was transpolar as observed by the DMSP/F6 satellite [Niedzwiedz *et al.*, 1989]. This stable arc had an electron density above  $10^5 \text{ cm}^{-3}$  in the  $E$  region. On March 1, 1987 we observed three polar cap arcs. Two of them were Sun-aligned and the other hook-shaped. The two Sun-aligned arcs were initially separated by 80 km with peak densities located at substantially different altitudes. They subsequently merged into a single broad arc. We discuss the properties of Sun-aligned arcs for these two nights to demonstrate repeatability of some basic characteristics.

In section 2 we identify a data-taking mode designed for such studies, and present Sun-aligned arc parameters directly observable by this technique. In section 3 we extend analysis of the ISR data to present important derived parameters. In section 4 we discuss the implications of these measurements, develop their interpretation, and identify their significance to understanding of the electrodynamics, thermal character, and energetics of the arcs. Finally, in section 5 we summarize the main conclusions from this study.

## 2. DATA-OBSERVING MODE AND DIRECT OBSERVABLES

The Sondrestrom incoherent scatter radar (66.987°N, 50.949°W, 74° Invariant Latitude), is situated 100 miles (160 km) inland from the west coast of Greenland. Its location at a very high magnetic latitude makes this station capable of probing the nighttime polar cap and examining the dynamics of polar Sun-aligned arcs [Carlson *et al.*, 1984; Robinson *et al.*, 1987; Mende *et al.*, 1988].

While it is difficult, if not impossible, to recognize Sun-aligned arcs with conventional ISR observing modes in the absence of coincident optical imaging data, it is possible to design a radar mode that can unambiguously recognize them. We describe the design here, illustrated in Figure 1. The design is based on what we know of their morphology from optical imagery. The essence of the design is simple. One wants to map the electron density profile and velocity field over an area, with the area large compared to the arc, and with time resolution short compared to the time for the arc to pass through the ISR field of view. Signal to noise considerations determine look elevation and area of coverage, and limit azimuth scan rates and cycle time resolution.

Variability in the motion and lifetime of S-A arcs [Weber *et al.*, 1989] also imposes some restrictions. For this reason we implemented the azimuthal sweeps (AZ) at two different speeds. One AZ scan was performed at a rapid scanning velocity, with the purpose of obtaining a snapshot of the electron density inside fast moving arcs. Two slow AZ scans swept 90° in 2 min, probing slower moving arcs and providing the line of sight (LOS) velocity and the number density with smaller error bars. Good horizontal transarc spatial resolution was also achieved (15 km at 150 km of altitude when pointed across the arc, and ultimately limited to the 2.5-km radar beam width smeared over the integration time when pointed along the arc). These measurements were complemented with an elevation (EL) scan (perpendicular to the anticipated arc direction) that gives the dependence of the geophysical parameters on altitude and distance across the arc. The scan sequence (shown in the bottom panel of Figure 1) was slow AZ-fast AZ-slow AZ-EL. For the data

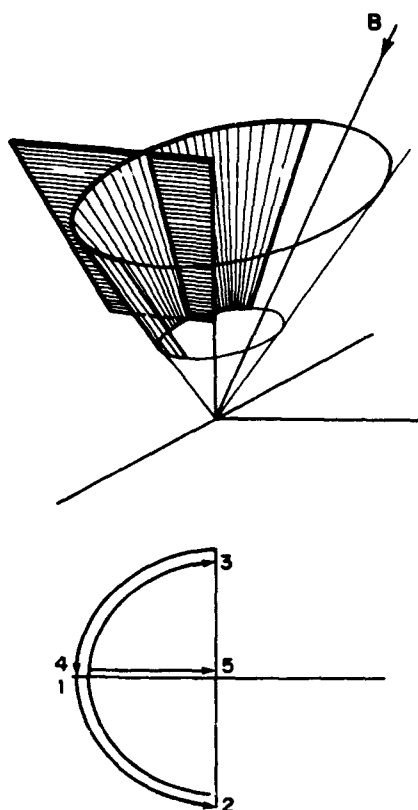


Fig. 1. Schematic representation of the volume scanned by the Sondrestrom radar during the EL and AZ sweeps of February 26, 1987. The bottom panel shows the sequence followed by the antenna. The initial azimuth was selected in order to align node 3 with the Sun-Earth direction.

presented here, one complete cycle was performed in 8 min and 40 s. Figures 2a-2h present the data corresponding to two consecutive cycles of this antenna pattern.

We will also show data from two other observing modes. One, tailored to a specific need, looked directly up the magnetic field line so as to give true instantaneous altitude profiles within a Sun-aligned arc. Such time continuous observations during the full passage of an overhead arc thus allow detailed diagnosis of the properties of a transverse section of an arc. These observations are presented in Plates 1a and 1b.

The third data set presented here, Figures 4a-4c, for March 1, 1987, again shows electron number density and LOS velocity. The antenna pattern consisted of a full 360° AZ scan and two 120° EL scans embedded at planes perpendicular to each other. By chance, a Sun-aligned arc is clearly apparent 150 to 200 km duskward (and westward) of the ISR on the Figure 4a scan, although the 20-min time resolution of this standard Sondrestrom observing mode is too slow to track or in general unambiguously recognize an arc. The Sondrestrom ISR is able to make a proper identification of polar cap arcs based upon (1) the ability of the radar to measure the number density and the LOS velocity while doing rapid scans, and (2) the well-known distribution of density gradients and velocity shears within the arcs [Carlson *et al.*, 1984]. Moreover, *E* region polar cap arcs exhibit enhanced densities below 200 km. Recall that chemical lifetimes are so short below 200 km that strong  $N_p$  enhance-

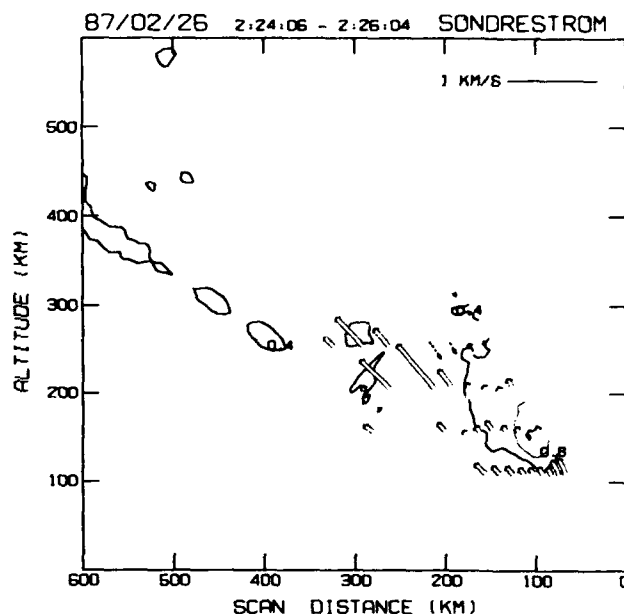


Fig. 2a. Number density contours and line of sight (LOS) velocity measured by the Sondrestrom radar on February 26, 1987 and during the time interval from 0224 to 0226. The azimuth was kept fixed at 231° and the elevation varied from 25° to 60°. The initial density contour corresponds to  $0.4 \times 10^5 \text{ cm}^{-3}$ , and consecutive contours increase linearly in steps of  $0.4 \times 10^5 \text{ cm}^{-3}$ . The LOS velocity was scaled in order to represent a velocity equal to 1 km  $\text{s}^{-1}$  as a segment 100 km long. The dashed line vectors indicate LOS velocities directed toward the radar, and the double line vectors characterize plasma motion away from the radar.

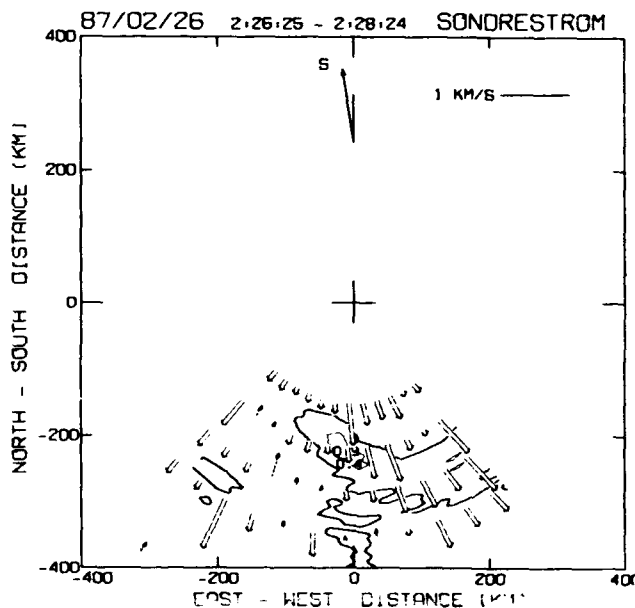


Fig. 2b. Plasma parameters corresponding to the AZ scan of 0226-0228. The constant elevation was 35° and the azimuth changed from 231° to 141°. The measured velocity and density have been projected to a horizontal plane using the same scaling factors employed in Figure 2a. Geographic north is at the top and west is on the left side of the plot. The arrow at the top central part indicates that during the experiment the direction of the Sun was 7° west of geographic north.

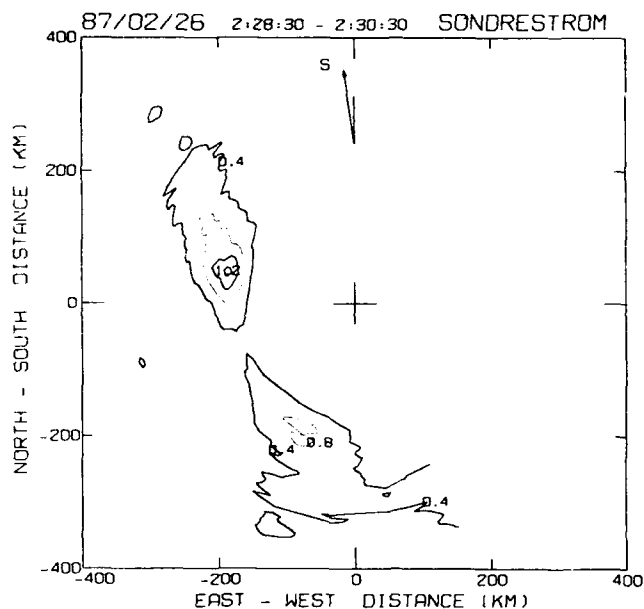


Fig. 2c. Plasma density for February 26, 1987 and time interval between 0228 and 0230. The antenna scanned  $180^\circ$  in 2 min using a fixed elevation of  $35^\circ$ . The scan started at an azimuth of  $141^\circ$  and ended at  $321^\circ$ . The measured LOS velocity is not shown in this plot.

ments identify local production of ionization. We have used the density and LOS velocity mapping capabilities provided by the AZ scans to properly determine the occurrence of arcs.

The densities plotted in Figures 2-4 and Plate 1 are on a linear scale. The initial value and the interval between consecutive levels are both equal to  $0.4 \times 10^5 \text{ cm}^{-3}$ . The arrows superimposed to the  $N_e$  contours represent the LOS

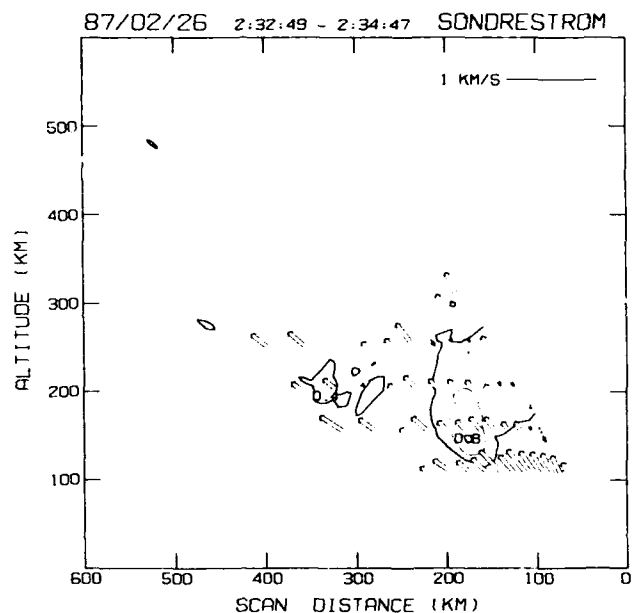


Fig. 2e. Similar to Figure 2a, but for the time interval 0232-0234.

velocities; they have different patterns and lengths according to the sign and magnitude of the LOS velocity. At 150 km of altitude the density and velocity statistical uncertainties were about 5% and  $<100 \text{ m s}^{-1}$  respectively.

#### 2.1. February 26, 1987 Scans

Data from this day show a stable Sun-aligned polar arc that stayed in the radar field of view for 40 min. This arc penetrated to the E layer ( $N_e$  was enhanced at altitudes as low as 120 km), and was detected near local midnight. Its southernmost region was observed to be merged to the poleward edge of the auroral oval during the early part of the

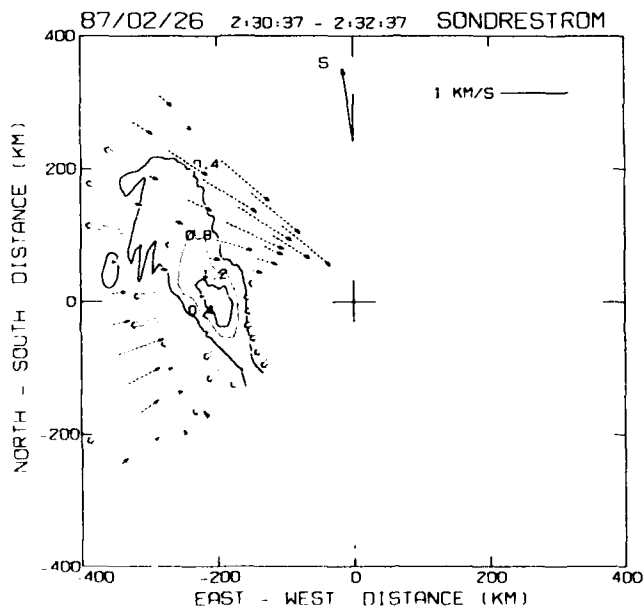


Fig. 2d. Top view of the density and the LOS velocity, both projected to a horizontal plane. The scan time is from 0230 up to 0232. This plot corresponds to the northern quadrant. The elevation is  $35^\circ$  and the scan starts at  $321^\circ$  of azimuth and continues until  $231^\circ$ . The scaling factor is the same as in previous figures.

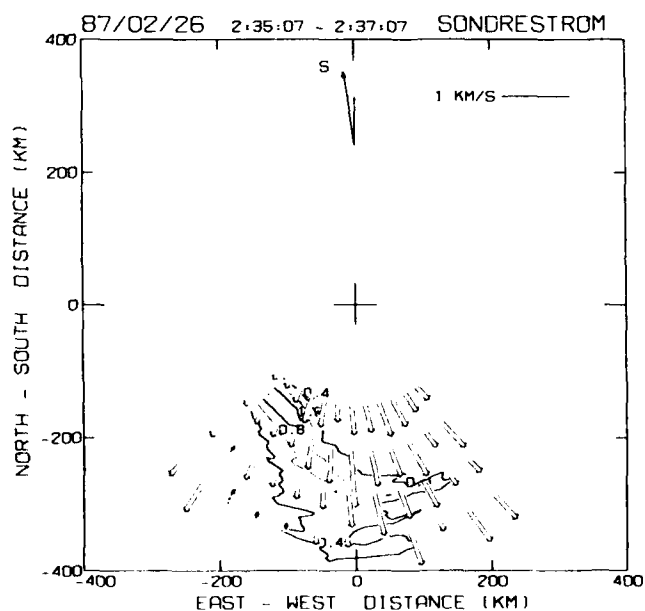


Fig. 2f. Similar to Figure 2b, but corresponding to the time between 0235 and 0237.

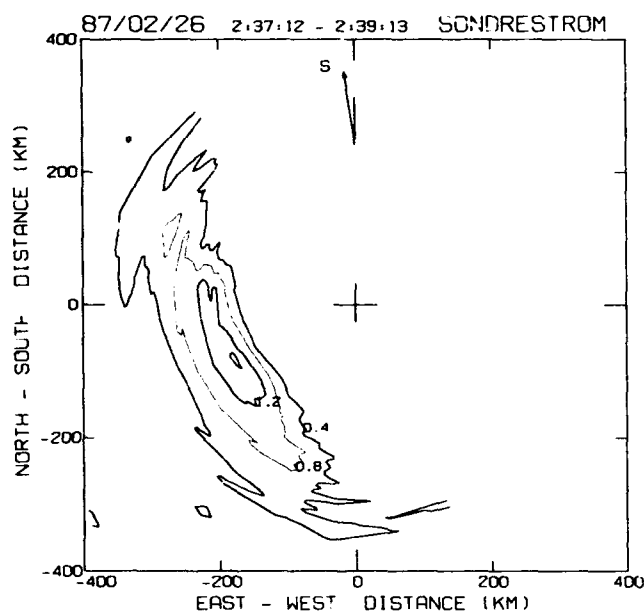


Fig. 2g. Similar to Figure 2c, but for time 0237.

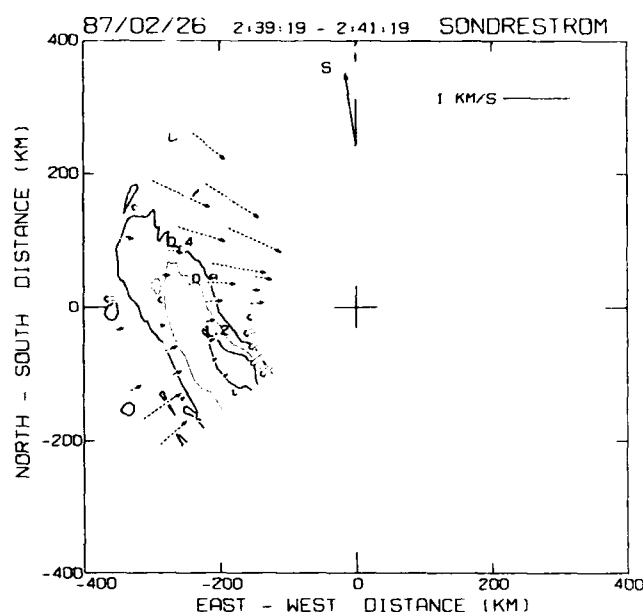


Fig. 2h. Similar to Figure 2d, but for time 0239.

arc transit. At the time of the experiment the background density in the polar cap  $F$  region was  $0.2 \times 10^5 \text{ cm}^{-3}$ , a value well below the lowest density contour level of Figure 2. The Pedersen conductivity peak values corresponding to each scan are presented in Table 1, which also includes the altitude, distance along the dawn-dusk meridian, and displacement velocity of both maxima. The geomagnetic  $K_p$  index was 1+ and the solar flux ( $S_a$ ) 73.9.

The data of Figure 2a were obtained between 0224 and 0226 UT when the S-A arc, as defined by scans of Figures 2b–2d, was located to the west of the radar station. The beam scanned through most of the arc, and also probed a duskward region beyond the arc (left side). In this region beyond the duskward and equatorward edge of the arc the LOS velocity was directed away from the Sun and radar (the small electron density in this region precludes measurement of a precise magnitude of the velocity). Within the arc, at  $F$  region altitudes (see range gates 2 and 3 placed at 160 and 210 km of altitude), the LOS velocities (looking transverse to the arc) were less than  $100 \text{ m s}^{-1}$ . That the density contours trace to lower altitudes in the dawn (right) side of the arc suggests harder precipitation there.

Figure 2b presents the data gathered with the slow AZ scan of 0226. Here, the Sun-aligned arc is identified by the high  $N_e$  structure seen in the lower south to southwest part of the plot, with an orientation much more clearly seen in Figures 2d, 2f, 2g, and 2h. The southern extreme of the arc shows (in Figures 2b, 2c, and perhaps 2f) a dawnside (eastward) extension with an electron density (about  $>0.5 \times 10^5 \text{ cm}^{-3}$ ) larger than the background  $N_e$  at altitudes about 200 km. This segment, not Sun-aligned, but more auroral oval-aligned, is probably associated with the connection of the Sun-aligned arc to the poleward edge of the auroral oval. The northern extreme of the Sun-aligned arc  $N_e$  contours mapped here in Figure 2b, all clearly pointing sunward, is determined by the simple geometry of the arc intersect with the conical radar scan.

Still in Figure 2b, gates 2 and 3, set at the same heights of

the previous EL scan, indicate a general antisunward motion and a shear inside the arc. Outside in the duskside there is a small sunward flow; conversely the dawnside region has a large antisunward flow. We will come back to this point in section 3, where we include the Earth corotation velocity and compute the direction of the plasma flow in the Earth-Sun frame of reference.

Figure 2c shows the same S-A arc during the fast AZ,  $180^\circ$  scan of 0228. The two quasi-ellipsoids that are observed represent the intersection of the arc and the cone generated by the azimuthal motion of the antenna (see Figure 1). The north and south cross sections of the arc have a maximum density of  $1.6$  and  $0.8 \times 10^5 \text{ cm}^{-3}$  respectively. The angle between geographic north and the arc alignment was equal to  $-23.5^\circ$ . The LOS velocity, in spite of being measured, is not presented here because of its poor statistical accuracy and its coarse spatial resolution following from the rapid radar scan.

Figure 2d shows the slow AZ scan that starts at 0230. The LOS velocity measured in the  $F$  region (second range gate) shows smaller values as the counterclockwise AZ scan progresses. At  $-90^\circ$  azimuth it changes from a toward orientation to a direction away from the radar. The LOS velocity corresponding to the  $E$  region (first gate) shows a similar characteristic, with the reversal occurring earlier in the scan. The statistical error of the LOS velocity measurement is  $20 \text{ m s}^{-1}$  for gate 1 and about  $50 \text{ m s}^{-1}$  for gate 2. In spite of the latter being a sizable error when the magnitude of the velocity is small, the velocity reversal can be visualized following the trend of the velocity values. At the end of the scan (southwest), gates 1 and 2 exhibit LOS velocities oriented away from the radar and with a value of order  $100 \text{ m s}^{-1}$ . The density contours indicated that the arc was oriented  $-30^\circ$  away from the north.

The second partial EL scan, in Figure 2e, measured the complete cross section of the arc, and also probed the dawnside region outside the arc (right side). The region of maximum density was found displaced 84 km toward mag-

TABLE 1. Motion of the S-A Arc Along the Dawn-Dusk Meridian

Type of Scan	Maximum Pedersen Conductivity, $\times 10^4$ mho/m	Time, UT	Altitude, km	Dawn-Dusk Displacement, km	Time Difference,* s	Distance Difference,* km	Velocity, Dawn to Dusk,† m s <sup>-1</sup>
EL	1.96	0225:26	129.9	107.6			
AZ	1.86	0226:45	125.3	152.6	79	45.0	569 (469)
AZ	2.43	0229:50	120.7	151.1	185	-1.5	-8 (-108)
AZ	1.95	0231:37	131.1	171.9	107	20.8	194 (94)
EL	2.20	0233:19	121.2	170.2	102	-1.7	-16 (-116)
AZ	3.60	0235:07	125.2	175.3	108	5.1	47 (-53)
AZ	2.89	0238:12	128.5	187.3	185	12.0	65 (-35)
AZ	2.84	0240:59	128.5	188.6	167	1.3	8 (-92)

\*Differences are relative to the preceding scan.

†Left-hand number Earth corotating frame, right-hand number Earth-Sun frame.

netic west from its previous location 9 min earlier (a dawn to dusk virtual velocity by the  $N_e$  contours of about  $150 \text{ m s}^{-1}$ ). The LOS plasma velocity within (and nominally transverse to) the arc was about  $150 \text{ m s}^{-1}$  in the  $F$  region and  $300 \text{ m s}^{-1}$  for the  $E$  region, a factor of 3 increase with respect to the velocities of Figure 2a. The  $F$  region LOS velocities in the dawnside of the Sun-aligned arc (right side of the plot) are the reverse of on the duskside, with a value equal to  $100 \text{ m s}^{-1}$ .

For altitudes below 150 km in the (production-recombination) chemical equilibrium region of the  $N_e$  profile (examination of the slope of, for example, the  $0.4\text{--}0.8 \times 10^5 \text{ cm}^{-3}$   $N_e$  contours of Figures 2a and 2e and Plate 1) we find the duskside slope entering the arc shallower than the dawnside slope leaving the arc. This suggests a gradual hardening of the precipitating electron flux across the arc from the leading edge to the trailing dawnside, where the greatest depth of penetration occurs. There is a relatively sharp cutoff of ionizing electron flux on the (trailing) dawnside of the arc. We cannot claim here a statistically significant sample (three out of the three cases of 0224, 0233, 0210 on February 26, 1987, and consistency for the fourth case of Figure 4c at 0340, March 1, 1987).

The difference in character (bifurcated versus continuous) between the  $N_e$  contours of Figures 2c and 2g is due to the geometry of the ISR conical scan intersecting the slab of arc ionization. This may be appreciated by visualizing a vertically elevated slab or small horizontal cylinder, either piercing the ( $55^\circ$  vertex angle) vertical conical surface and passing through near its axis, or grazing (and encompassing a portion of) the conical surface to one side. Thus the intersection of a conical scan with Sun-aligned cylindrical forms will depend on the distance of the axis of the horizontal cylinder from the vertical axis of the cone, and will look very much like Figures 2d, 2f, 2g, and 2h. The intersection of a conical scan with a horizontally stratified ionosphere is a set of concentric circle  $N_e$  contours. Figures 2b and 2c show Sun-aligned arc contours merging to the southwest with some horizontally stratified ionospheric plasma. The core ionization in Figure 2 ( $\approx 0.8 \times 10^5 \text{ cm}^{-3}$ ) is continuous, Sun-aligned, and quite stable in density, size, and height (e.g., Figures 2a and 2e), and separates  $F$  region plasma flowing away from the Sun on its dawnside from plasma flowing much more slowly and toward the Sun on its duskside (the plasma is predominantly antisunward within this arc).

Several characteristics of the measured LOS velocity and the number density associated with the arc of February 26

can also be explained by changes in the relative location of the arc with respect to the radar. The small LOS velocity of Figure 2d at  $-90^\circ$  azimuth is interpreted as a near perpendicularity between the flow and the sight direction. The differences in the peak density observed on consecutive AZ scans or during two sectional cuts of the same arc (Figure 2c) are due to variations in the distance between the radar and the S-A arc.  $E$  region velocities collected during the AZ scans can be used to reassure that the null LOS velocity is due to a near perpendicularity of the flow and the sight direction. The velocity in the  $E$  layer, being smaller and rotated clockwise with respect to the  $F$  region flow, will give a null LOS velocity at a different look angle, as in Figure 2d.

Figure 3 shows the density contours of Figures 2d and 2f superimposed to the OI (6300 Å) emissions (hatched region) recorded simultaneously by the GL all-sky imaging photometer. Both radar and optical data sets have been transformed and scaled to a common coordinate system that depicts geographic latitude and longitude. The red line optical aurora was assumed to originate at 200 km of altitude. The emission produced by impact excitation shows a bright, discrete, and isolated feature located westward of the radar station. The number density contours measured by the ISR mostly overlap the hatched region, except for a small part to the south. This region may correspond to the oval  $F$  layer. Figure 3 confirms genuinely and unambiguously that the radar, in fact, diagnosed an arc which was Sun-aligned and locally produced.

## 2.2. February 26, 1987 Dwells

Plates 1a and 1b show observations of the same stable and energetic arc as in Figure 2, obtained between 0204 and 0222 as the arc passed overhead the antenna parked in the direction up **B**, the magnetic field. An integration time of 1 min was selected in order to provide temperature error bars smaller than 10% at a 200-km altitude. The arc motion across the radar beam cannot be assumed constant. However from Figures 2a–2h (see Table 1) we know that the Sun-aligned arc moved westward (toward dusk) at order of  $100 \text{ m s}^{-1}$  in the Earth corotating frame. As a result of this motion, the duskside of the arc appears earlier (lefthand side) in Plates 1a and 1b. Color-coded vertical profiles of  $T_i$  and  $T_e/T_i$  are superimposed on the density contours in Plates 1a and 1b, respectively. In the center of the arc the ion temperature is 500 K in the  $E$  layer and about 700 K at  $F$  region heights.  $T_i$



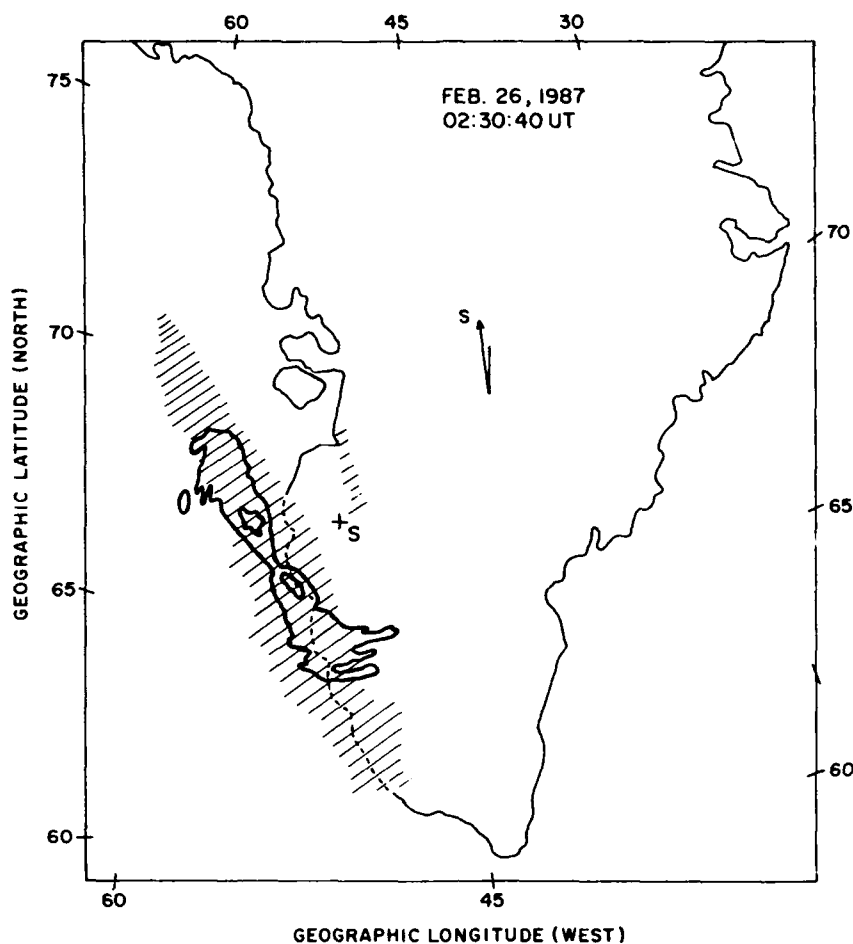


Fig. 3. Schematic representation of the auroral luminosity observed by the GL/ASIP on February 26, 1987. The number density measured by the Sondrestrom ISR is superimposed as a thick line contour. The two contour levels correspond to  $0.4$  and  $1.2 \times 10^5 \text{ cm}^{-3}$ . Both  $6300 \text{ \AA}$  intensities and radar  $N_e$  have been transformed to geographic coordinates. They are both colocated and aligned in the same direction (about  $24^\circ$  west of north).

sharply increases in the dawnside of the arc reaching  $1300 \text{ K}$  and exceeding  $T_e$  at both  $E$  and  $F$  layers. The electron temperature has a different pattern, with  $T_e$  enhancements of  $500 \text{ K}$  colocated with regions of higher bottomside electron densities (more intense precipitation). This behavior is reflected in Plate 1b, where the  $T_e/T_i$  ratio is observed to decrease from  $>1.5$  to  $0.8$  near the dawn edge boundary. The S-A arc, defined by the  $0.8 \times 10^5$  contour, drifted across the radar beam in  $10 \text{ min}$ . If we take the average westward speed to be of order  $100 \text{ m s}^{-1}$  in the Earth frame, which implies a width of about  $60 \text{ km}$  for the S-A arc, we get reasonable agreement with the  $0.8 \times 10^5$  contours of Figure 2. The maximum density was  $1.9 \times 10^5 \text{ cm}^{-3}$  at  $130 \text{ km}$  of altitude. The width of the arc and the number density are both consistent with the view that the arc properties are rather stable over the time period covered by Figure 2 and Plate 1 (over half an hour).

### 2.3. March 1, 1987

To demonstrate that the conclusions to be reached from the February 26 data do not represent a unique circumstance, we present data for another Sun-aligned arc of comparable intensity, observed three nights later. On this night a system formed by two Sun-aligned arcs traversed the

Sondrestrom field of view while the radar performed a 20-min sequence of AZ-EL-EL scans. (At this time the  $K_p$  and the solar flux indices were  $2+$  and  $72.8$  respectively).

Figure 4a shows the number density and the LOS velocity measured with the full circular AZ scan of 0324 with the antenna at a fixed elevation of  $45^\circ$ . Most of the patchy features to the east and south of the station are radar intersections of the polar cap  $F$  region. The elongated trace located  $135 \text{ km}$  westward of the radar is the clear signature of a S-A arc. We have already noted that any significant ionization enhancement near  $150 \text{ km}$  is due to ongoing ionization, and will have attendant impact-excited optical emissions. Thus we must say something about the oval electron density enhancements approximately  $80 \text{ km}$  east of the northern and southern extremes of this elongated trace. These have electron density, electron temperature, and electrodynamic consistent with Sun-aligned arc signatures (piercing rather than grazing the conical radar scan). However, the ISR alone cannot unambiguously identify that they are connected by continuous Sun-aligned enhanced electron density contours, and thus they will not be discussed further in this paper.

A pair of EL scans (Figures 4b and 4c) cut this arc system, respectively in its northwest and southwest regions, 8 and 14

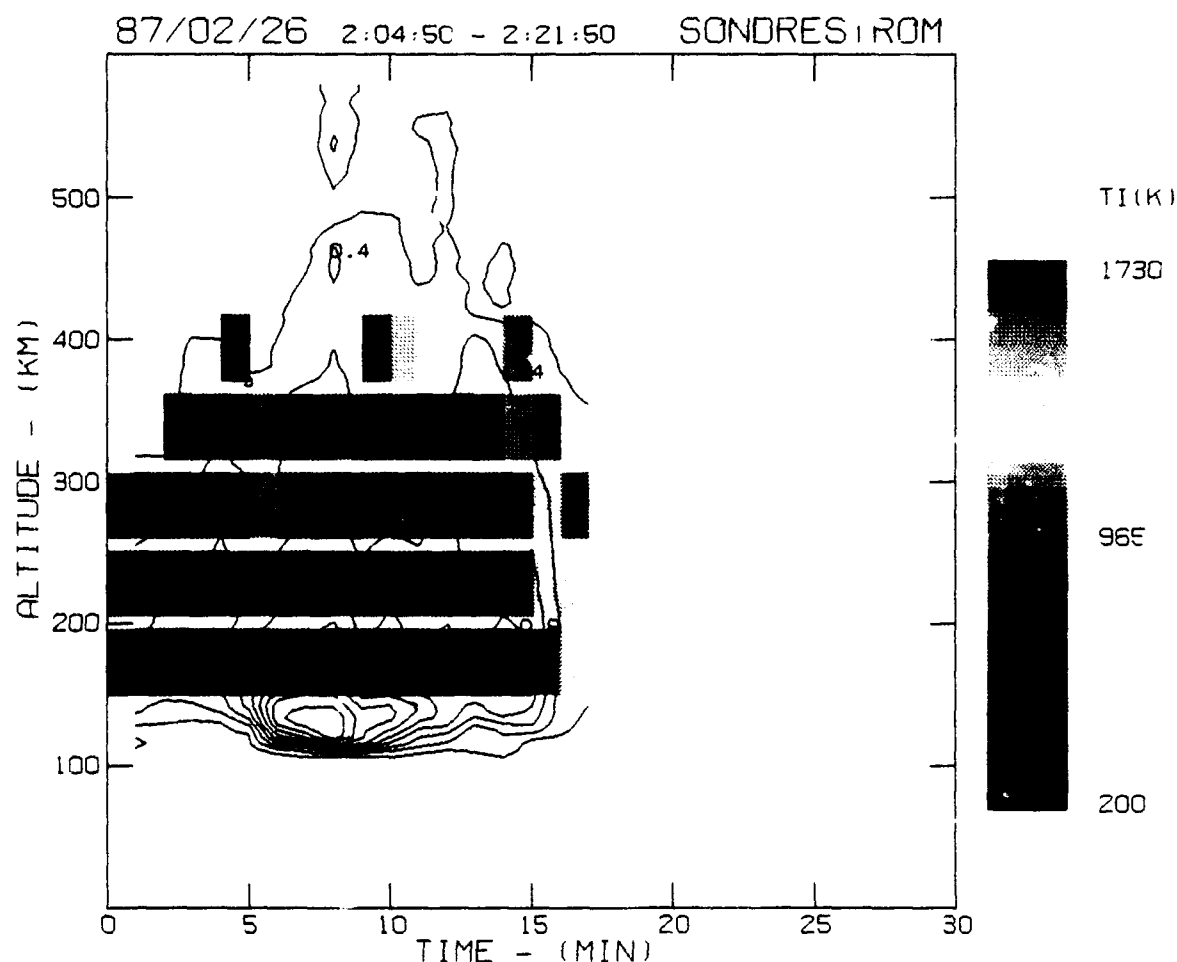


Plate 1a. Color-coded representation of the ion temperature as a function of altitude and time for February 26, 1987, time interval from 0204 to 0221. The  $N_p$  contours, measured simultaneously, are superimposed. The antenna was pointing parallel to the local  $B$  lines ( $EL = 80^\circ$ ,  $AZ = 141^\circ$ ). Each individual profile is the result of 1-min integration time. Density contours start at  $0.2 \times 10^5 \text{ cm}^{-3}$ .

min after it was mapped by the AZ scan. An ionization feature to the northeast is seen at 0343 on the EL scan at  $51^\circ$  azimuth. This (soft ionizing flux) feature is not a stable Sun-aligned arc, as it does not extend into the southeast radar scan. This will be discussed later.

The right side of Figure 4b (southern distances) shows the LOS velocity at 160 km of altitude (gate 2) varying as expected if the velocity is constant and the variation is produced only by changes in the radar look angles. A different behavior is observed in the northern part (left side) of the plot, where the LOS velocities increase abruptly and then start decreasing at  $\sim 100$  km of distance. The region of larger LOS velocity coincides with the downward edge of the arc.

### 3. DATA ANALYSIS

This section presents the analysis of the data corresponding to February 26 and March 1, 1987. Here, we describe the method that was used to calculate the velocity vector, the Hall and Pedersen conductivities, the electric field, the horizontal and the field-aligned currents, the vertical component of the Poynting flux and the ion-neutral differential temperature. The data acquired during the EL and AZ scans

have been processed independently using different algorithms (Sections 3.1 and 3.2) which were tailored respectively for each of these two types of scans. The results of these independent calculations provide mutually consistent values of the geophysical parameters, lending further confidence to the analysis procedures and results.

#### 3.1. Analysis of Elevation Scans

At  $F$  altitudes the plasma drifts in the  $\mathbf{E} \times \mathbf{B}$  direction. In the  $E$  layer the large ion-neutral collision frequency prevents the ions from moving perpendicular to  $\mathbf{E}$ . Brekke *et al.* [1973, 1974] used the relation between winds, drifts and electric fields to obtain the  $E$  region neutral winds. They employed ion velocity vectors measured at two different altitudes but connected by the same field line.

A different approach was exercised by Doupnik *et al.* [1977] and de la Beaujardiere *et al.* [1977] in which simultaneous LOS velocities measured from the  $E$  and  $F$  layers and the radar-deduced wind velocity were used to determine two components of the velocity vector; the third component (parallel to  $\mathbf{B}$ ) was assumed to be null.

Nevertheless, the ion motion along  $\mathbf{B}$  is seldom zero. Mechanisms such as adiabatic expansions, parallel electric

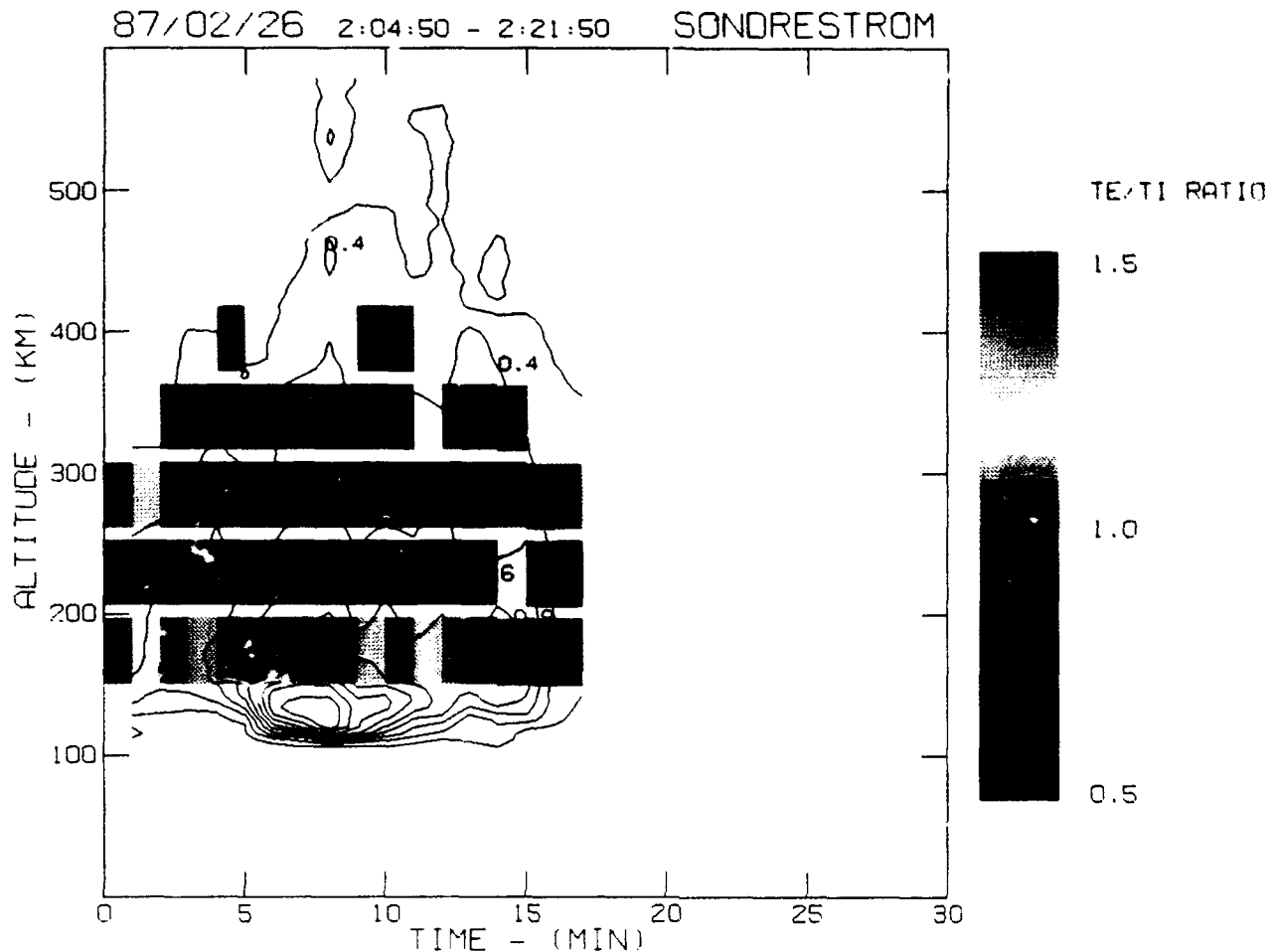


Plate 1b. Similar to Plate 1a, but the color-coded diagram represents the temperature ratio ( $T_e/T_i$ ). The time is the same as in the previous figure.

fields or the small component of the neutral wind along **B**, all drive ion motions along magnetic lines. *Spencer et al.* [1976] detected vertical neutral winds in the auroral zone, less than or of the order of  $80 \text{ m s}^{-1}$ . *Petcherich et al.* [1985] observed values of  $15 \text{ m s}^{-1}$  associated with auroral arcs. Here we measure the magnitude of the ionic motion in the direction parallel to **B** by pointing the antenna along **z** on February 26, 1987 between 0204 and 0222, before the sequence of EL and AZ scans and during the overhead transit of the arc.  $V_z$  was found equal to  $25 \pm 7 \text{ m s}^{-1}$ . In general a nonzero  $V_z$  will introduce an error equal to  $V_z \times \tan(\text{EL})$ . Consequently the null  $V_z$  assumption fails when the radar is directed near the up **B** position.

The velocity vectors were derived using the algorithm described in Appendix A. This method has some of the characteristics of the one employed by *Doupnik et al.* [1977], with the main difference that the input data were collected by EL scans instead of dwells. Appendix A also includes a description of the pulse configuration that was used, and a list of the different constraints which curtail the capability of the radar to measure the ionospheric parameters.

Concurrently with the radar, a Fabry-Perot interferometer recorded the intensity and the Doppler velocity of OI (6300 Å) emissions at the zenith and four cardinal points (J. Meriwether, personal communication, 1988). The neutral wind pattern measured on February 26, 1987 has been

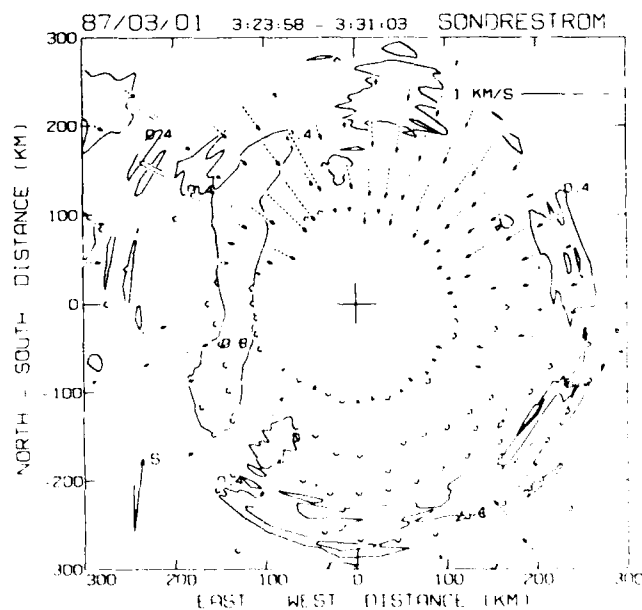


Fig. 4a. Number density and LOS velocity corresponding to March 1, 1987. The time interval is between 0323 and 0331. The antenna scanned 360° in about 7 min; the elevation was maintained fixed at 45°. The Sun direction is indicated in the lower left corner of the plot.

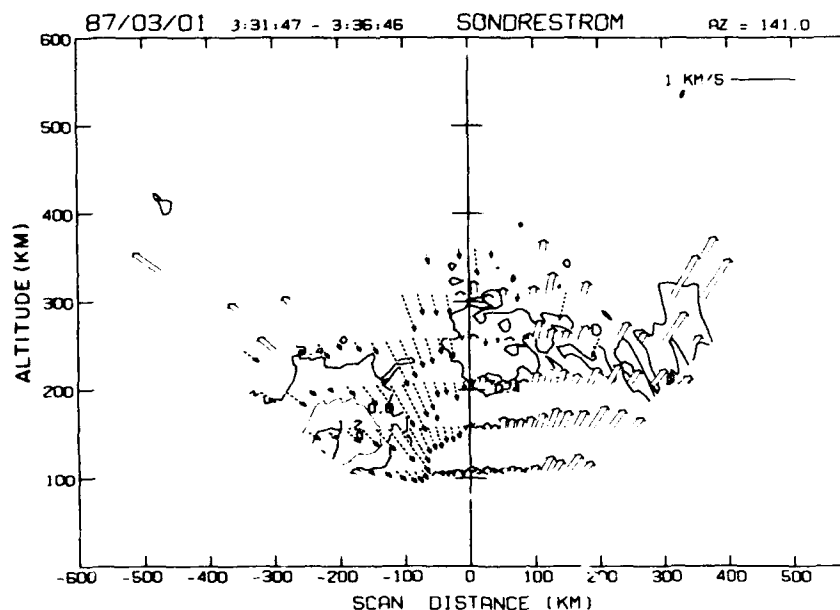


Fig. 4b. Elevation scan performed in the plane of the magnetic meridian between 0331 and 0336. Magnetic north is at the left side of the plot. Only arc A was probed by the radar during this scan.

described by *Niciejewski et al.* [1989]. They showed that the direction of the wind was southerly during the zenithal transit of the arc.

For all the data presented here, we have performed a complete velocity vector analysis, including actual measured neutral winds, and a three-dimensional magnetic field model. The results of the velocity analysis for the two EL scans of Figure 2 are displayed in Figures 5c and 6c. Here we present the resolved vectors and their error bars (dashed line). Geographic north is at the top of the panel and the arrow in the upper part points toward the Sun location. The top panels of these figures show the height-integrated Pedersen

and Hall conductivities plotted as a function of westward distance from the radar. Both Hall and Pedersen conductivities were calculated using the radar-measured number density, the *Schunk and Walker* [1970] expression of the ion-neutral collision frequency, and the *Banks and Kockarts* [1973] expression of the electron-neutral collision frequency. The neutral densities are from the MSIS-86 model [*Hedin*, 1987].

Figure 5 corresponds to the EL scan of 0224. During this time the Pedersen conductivity peaked at a horizontal distance of 105 km away from the radar, the Hall conductivity at 95 km. The three vectors farthest to the west have very

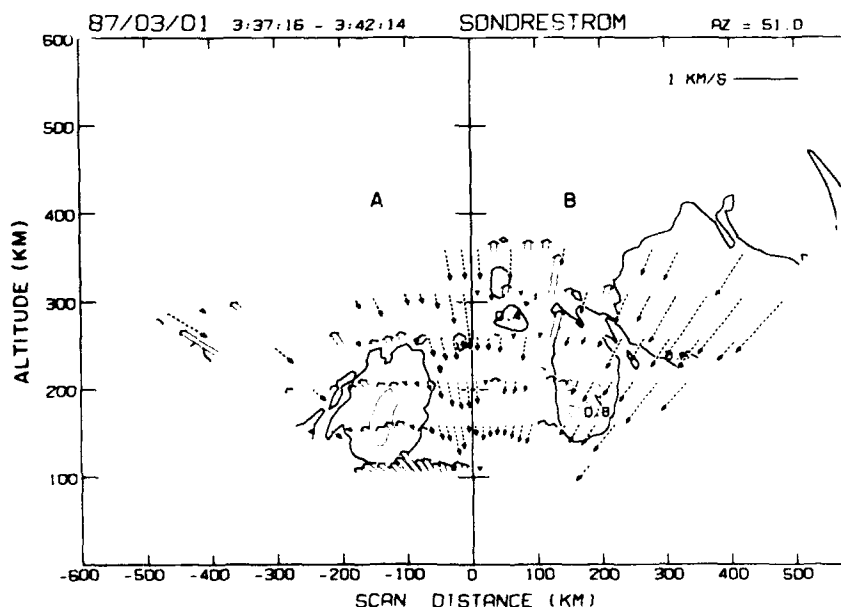


Fig. 4c. Same as Figure 4b, but for the elevation scan in a plane perpendicular to the magnetic meridian. The cross sections of both arcs are displayed at -180 and 150 km. The polar cap F region is on the right side of the plot at altitude of 300 km.

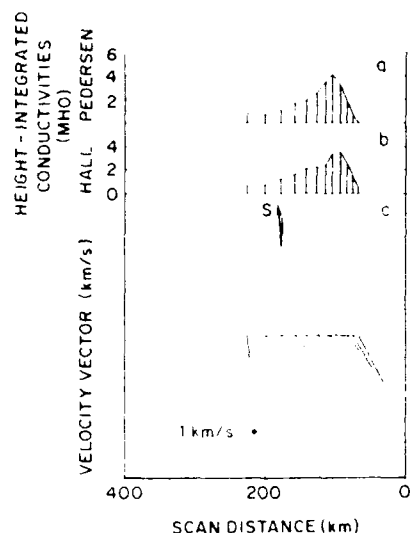


Fig. 5. Plasma parameters deduced from the data corresponding to the EL scan of 0224 on February 26, 1987 (Figure 2a): (a) Height-integrated Pedersen conductivity; (b) height-integrated Hall conductivity; (c) the velocity vectors calculated from the LOS velocity measured at  $E$  and  $F$  region altitudes as described in the text. The arrow at the middle of Figure 5c points, in geographic coordinates, to the direction of the Sun.

large uncertainties and are given least statistical weighting. On the contrary, the velocities closer to the arc have small error bars because of the higher  $N_e$ . These vectors show a very consistent antisunward flow. The magnitude of the velocity varies from less than  $100 \text{ m s}^{-1}$  at the center of the arc up to  $900 \text{ m s}^{-1}$  in the limits of the EL scan. The region of large conductivities coincides with the small ( $< 100 \text{ m s}^{-1}$ ) velocities. The sharp decline of the conductivities in the dawnside (right side) of the arc is partially due to our limited EL scan, which did not probe the  $F$  region at distances close to the radar.

Figure 6 shows the velocity vectors from the analysis of Figure 2c (0232). At this time the region of maximum

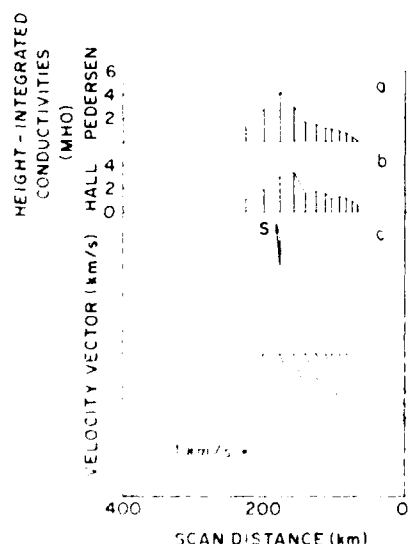


Fig. 6. Same as in Figure 5, but for the EL scan of 0232 (Figure 2c).

Pedersen conductivity was located at 175 km ground range from the station and the Hall conductivity peak at a horizontal distance of 155 km. Similar to Figure 5, the velocity shows a steady antisunward flow. Besides, the region of velocity gradients is extended in the dawnside of the arc reaching a value of  $1484 \text{ m s}^{-1}$  and then, slightly decreasing when the Pedersen conductivity returns to its background level of 0.2 mhos. Our results agree with those of Robinson *et al.* [1987] and Mende *et al.* [1988].

The unchanging characteristic of both Pedersen and Hall conductivities during two EL scans separated by 8 min argues in favor of this S-A arc being very stable with no appreciable variation of its source and dynamics. Based on the steadiness of this arc, we proceeded to merge the data of Figures 5 and 6 and form the three upper panels of Figure 7. This new set of velocity vectors and conductivities was used to compute the height-integrated and field-aligned currents following the expressions given by Brekke *et al.* [1974] and de la Beaujardiere *et al.* [1977].

$$\mathbf{J} = \sum_P \mathbf{E}_\perp + \sum_H \mathbf{E}_\perp \times \mathbf{B} B + \sum_P \mathbf{U}_\parallel \times \mathbf{B} + \sum_H (\mathbf{U}_\parallel \times \mathbf{B}) \times \mathbf{B} B \quad (1)$$

$$j = \nabla \cdot \mathbf{J}_\parallel \quad (2)$$

where  $\mathbf{J}_\perp$  and  $j$  are the current perpendicular and parallel to  $\mathbf{B}$ ,  $\sum_P$  and  $\sum_H$  are the height-integrated Pedersen and Hall conductivities.

The geophysical parameters and their error bars shown in Figures 7d–7g were all calculated in a coordinate system for which the  $+X$  axis is perpendicular to the arc alignment and directed toward dawn. The  $+Y$  axis is parallel to the arc and points sunward (poleward). The orientation of the arc was determined from the AZ scans displayed in Figures 2b–2h. It was found that the angle between the arc alignment and geographic north is equal to  $-24 \pm 5$ . The direction of the sun is  $7^\circ$  west of north.

Figure 7d shows the component of the electric field perpendicular to the arc  $E_\perp$  (component of the velocity along the arc).  $E_\perp$  is less than  $12 \text{ mV m}^{-1}$  in the duskward edge of the arc. It reaches its minimum value of  $5.4 \text{ mV m}^{-1}$  in the region of maximum conductivity. Then, it gradually increases in the dawnside until it presents a peak value of  $72 \text{ mV m}^{-1}$  at 94 km eastward from the center of the arc.  $E_\parallel$ , plotted in Figure 7e, has a different behavior. It remains constant and below  $6 \text{ mV m}^{-1}$  except for a region (distant 73 km from the center) in the extreme dawnward end of the arc, where  $E_\parallel$  increases to  $28 \text{ mV m}^{-1}$ .

Both components of the height-integrated horizontal currents are plotted in Figures 7f and 7g.  $J_\perp$  (transverse component) is proportional to  $E_\perp$ ; it is directed toward dusk and has a maximum value of  $0.096 \text{ A m}^{-1}$ .  $J_\parallel$ , the component along the alignment, presents two different regions. Dawnward from the center of the arc the average current is  $0.058 \text{ A m}^{-1}$ . Duskward,  $J_\parallel$  is below the uncertainty level of  $0.008 \text{ A m}^{-1}$ .

Considering that the  $\mathbf{E}$  field and the conductivities do not vary along the arc alignment,  $j$  is given by

$$j = E_\perp \frac{\partial \sum_P}{\partial X} + E_\parallel \frac{\partial \sum_H}{\partial X} + \sum_P \frac{\partial E_\perp}{\partial X} + \sum_H \frac{\partial E_\parallel}{\partial X} \quad (3)$$

The parallel current associated with the arc of February 26, 1987 was calculated following (3). The numerical deriv-

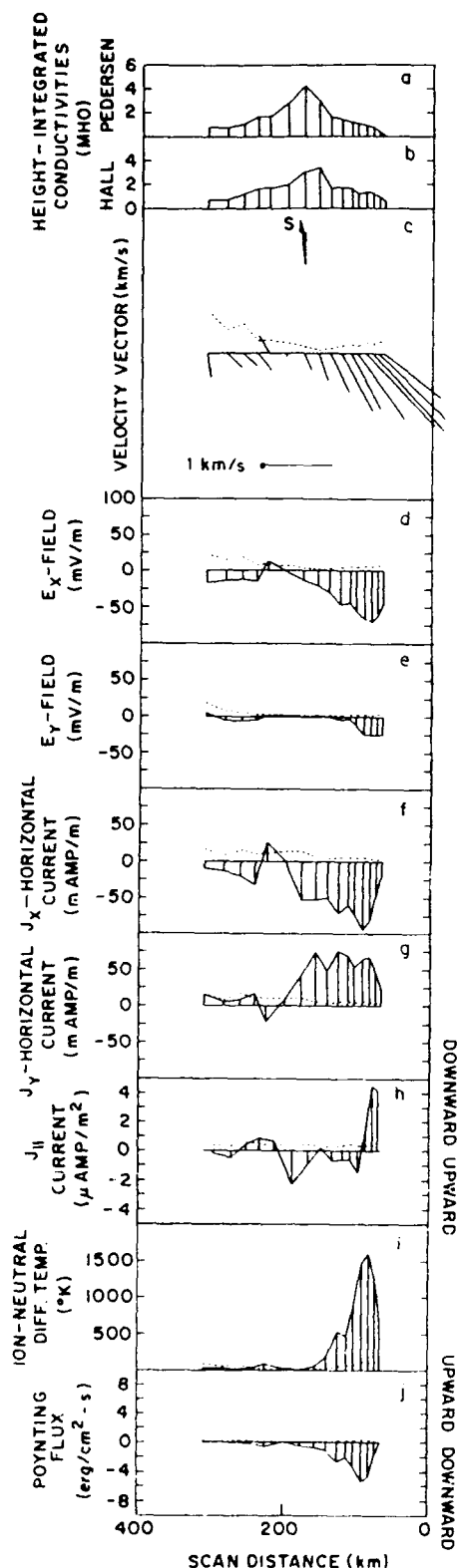


Fig. 7. Geophysical parameters which were derived using the conductivities and velocity vectors of both EL scans of February 26, 1987 (Figures 2a and 2e): (a) Pedersen conductivity; (b) Hall conductivity; (c) velocity vectors; (d) x component of the E field and the statistical error inherent to the measurement; (e) same as Figure 7d for y component; (f) x component of the height-integrated horizontal current; (g) y component of the height-integrated horizontal current; (h) field-aligned current density; (i) ion-neutral differential temperature computed from the measured ion and neutral velocity; and (j) vertical component of the Poynting flux.

atives were obtained by fitting a second-order polynomial to four consecutive values of  $E_x$  and  $E_y$ . In Figure 7h, downward currents are plotted as positive numbers. The second and fourth terms of the right side of (3) produce very small contributions to  $j_{\parallel}$  and can be neglected. In the duskside, the parallel current is less than  $1 \mu\text{A m}^{-2}$ . In the region of maximum conductivity,  $j_{\parallel}$  is directed upward with an average value equal to  $1 \mu\text{A m}^{-2}$ . Between 156 and 140 km  $j_{\parallel}$  decreases to a level near zero. This decrease is due to a large ( $+2 \mu\text{A m}^{-2}$ ) current originated by a negative gradient of the Pedersen conductivity, first term in the right-hand side of (3).

The temperature enhancements of the ion gas observed on the dawnside of the arc are colocated with regions of large plasma flow. This fact led us to calculate the frictional heating due to the ions being dragged through the neutral gas by an electric field. Fedder and Banks [1972] have indicated that ion temperature effects can be described by the ion energy equation. In the steady state  $T_i$  depends on the vector difference between ion and neutral velocities [Baron and Wand, 1983]. Hence, if ions transfer momentum to the neutrals sufficiently rapidly that the neutral particles approach the ion velocity, only modest  $T_i$  enhancements will occur. Following the derivation of Baron and Wand [1983] for momentum transfer, we found that for the number density of the S-A arcs analyzed here the time constant is several hours, so for large ion velocities, large  $T_i$  enhancements and heating rates should occur. We have used the radar ion velocity of Figure 7c and the neutral velocity from the FPI to calculate the ion-neutral differential temperature shown in Figure 7i. Our calculations show that between the dusk and the center part of the arc the differential temperature is less than 100 K. Substantial  $T_i$  enhancements occur on the dawn edge, up to 1600 K here. This is simply because this is where the largest ion velocities occur, while the neutral particles do not have time to experience significant acceleration.

Poynting's theorem states that the rate of energy flow per unit area is equal to  $E \times \delta H$ . Here, we present the calculation of the vertical component of the Poynting flux ( $P_z$ ) which was computed using the electric field and the horizontal current obtained solely from radar measurements. Following Ampere's law and the current continuity equation (2) and assuming that (1) only the field-aligned current sheets contribute to  $\delta H$ , and (2) the magnitude of the total downward  $j_{\parallel}$  current is equal to the magnitude of the upward  $j_{\parallel}$  (they are considered to be closed by horizontal Pedersen currents), the  $P_z$  is nonzero within the arc and given by

$$P_z = -E_{\parallel}(J_x - \langle J_x \rangle) \quad (4)$$

where  $\langle J_x \rangle$  is the average value of the horizontal current measured at the dawn and dusk boundaries of the S-A arc. Figure 7j displays the values of  $P_z$  calculated according to this simple algebraic relation. Negative values refer to a downward energy flux. The region of more intense precipitation has a small Poynting flux,  $<1 \text{ erg cm}^{-2} \text{ s}^{-1}$ . However,  $P_z$  is maximum, about  $5 \text{ erg cm}^{-2} \text{ s}^{-1}$  further east of the arc, on the dawnside and coincident with the region of maximum  $E_{\parallel}$  field. Consistency with these findings can also be claimed from less direct calculations (E. J. Weber, private communication, 1989) which lead to similar findings of a downward Poynting flux on the dawnside of a Sun-aligned arc diagnosed by a rocket flight [Weber et al., 1989]. The time span for that segment of rocket data, however, was short com-

pared to an Alfvén bounce period, so temporal variation cannot be excluded from those data, whereas the ISR data here show steady conditions.

The arc cross sections of Figure 2 were also used to determine the motion of the S-A arc. The enhanced electron density profiles measured by the radar were transformed to Pedersen conductivity profiles. The maximum  $\sigma_p$  value corresponding to each scan is tabulated in Table 1. The numbers in parentheses in the last column refer to the arc motion along a dawn-dusk meridian in a frame fixed with the Sun-Earth frame of reference (positive numbers represent duskward velocities). The arc velocities show some scatter. However, the general trend is a duskward motion of  $460 \text{ m s}^{-1}$  before 0227 UT followed by a dawnward drift of  $60 \text{ m s}^{-1}$ .

Figure 8 presents the derived geophysical parameters for the EL scans of March 1, 1987. This figure has the same format of Figures 5, 6, and 7. However, when the statistical uncertainty of the velocity was large or the antenna was pointing close to the up *B* position the parameters were deleted from the plot.

Figure 8 shows the derived parameters for the EL scan that was performed along the magnetic east-west. Both Pedersen and Hall conductivities present two peaks corresponding to both arcs of Figure 4c. The background conductivity was 0.3 mhos. Both arcs were located at regions of large velocity gradients where  $\nabla \cdot \mathbf{E} < 0$ . However, one of them (arc B, see Figure 4c) had a sunward flow and the other had an antisunward convection. Figure 8, as well as Figure 7, shows the anticorrelation between the magnitude of *E* and the conductivities. This means that a near-zero *E* field occurs when the densities are the largest. The *Y* component of *E* is only  $-4 \text{ mV m}^{-1}$  in the center and dawnside of arc A. The *E<sub>x</sub>* component varies from a peak value of  $-90 \text{ mV m}^{-1}$  in the dawn edge of arc A to  $-120 \text{ mV m}^{-1}$  in the dusk boundary of B. *J<sub>x</sub>* is proportional to *E<sub>x</sub>* with a maximum value near  $0.1 \text{ A m}^{-1}$ . *J<sub>y</sub>* reaches values up to  $0.075 \text{ A m}^{-1}$ . The field-aligned current is upward ( $2 \mu\text{A m}^{-2}$ ) in the region of arc A; *j<sub>z</sub>* is downward in the duskside of arc B, reversing to the highest upward value of this plot ( $4 \mu\text{A m}^{-2}$ ) at the center of arc B. The ion-neutral differential temperature of Figure 8i and the Poynting flux of Figure 8j show enhanced values at the boundaries of arcs A and B.

### 3.2. Analysis of Azimuthal Scans

Figure 9 presents the velocities which were obtained following the method outlined in Appendix B. We used data from the four partial AZ scans of Figures 2b, 2d, 2f, and 2h. This figure is in geographic coordinates, where the light traces refer to antisunward convection and the heavy traces indicate sunward flow. The vectors corresponding to each scan were shifted along the dawn-dusk meridian in order to compensate for any displacement of the S-A arc which occurred between the scans. We also averaged the velocity vectors when two or more vectors were located within  $\pm 20 \text{ km}$  from each other.

The vector velocities of Figure 9 reproduce (verify) many of the characteristics that were obtained from the analysis of the EL scan data. Furthermore, they present additional features which were not resolved by the limited coverage of the EL scan. The common features are as follows: (1) There is the large antisunward velocity in the dawnside of the arc

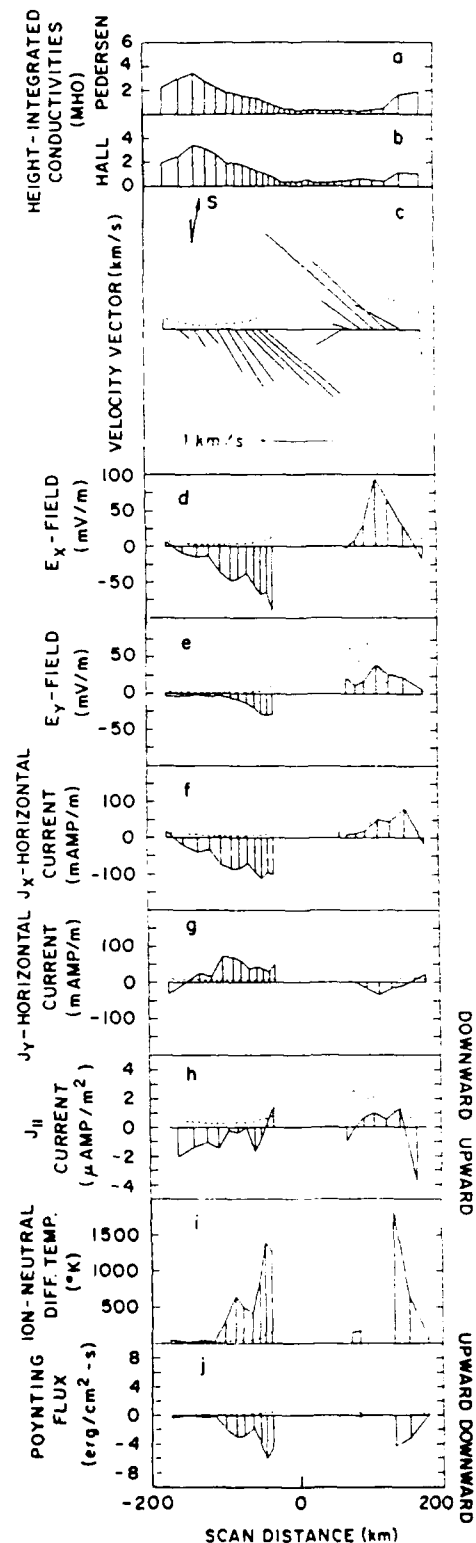


Fig. 8. Same as Figure 7, except that it corresponds to time 0337 of March 1, 1987.

with a peak value near  $1200 \text{ m s}^{-1}$ . (2) The region of velocity gradients with negative divergence has a width of about  $175 \text{ km}$  measured along the dawn-dusk meridian. (3) Antisunward velocity decreases beyond the dawn edge of the arc. (4) There is a high degree of consistency during consecutive

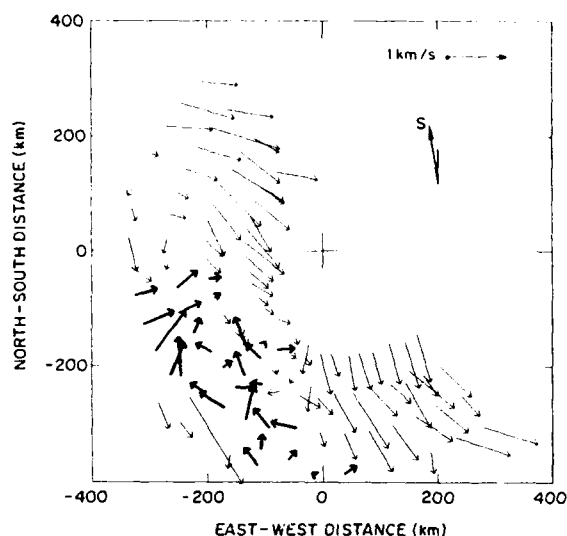


Fig. 9. Velocity vectors obtained from the four slow AZ scans of February 26, 1987. A  $1 \text{ km s}^{-1}$  vector is represented as a segment 100 km in length. The inclination of the vector indicates the direction of the flow.

antenna cycles. The new signatures are as follows: (1) The duskside of the arc presents a strong sunward flow, with a peak value of  $500 \text{ m s}^{-1}$ . (2) The region of sheared flow follows the arc alignment in the area covered by the scan (about 700 km). (3) The antisunward flow in the dawnside shows that beyond the first-order constancy of plasma flow parallel to the arc, there is a gentle second-order variation along the alignment of the arc. The magnitude of the vectors decreases from  $1200 \text{ m s}^{-1}$  in the poleward part of the scan to  $900 \text{ m s}^{-1}$  in the equatorward region. (4) The northern part shows only a gradient but not a reversal. (5) Near the center of the plot the sunward flow shows a rotational reversal which suggests the limit of the sunward motion. (6) Further duskward from the region of sunward convection, the flow is again antisunward. There is a sharp shear with positive divergence. (7) The width of the sunward flowing region is of order 100 km.

### 3.3. Analysis of Data Collected With the Antenna Directed Up **B**

Derived parameters of the data collected during the dwells of February 26, 1987 are shown in Figure 10, together with the Poynting flux and Joule heating rate from the EL scans. Figures 10a, 10b, 10c, and 10e correspond respectively to the Pedersen conductivity calculated from the number density obtained from the overhead transient of the arc, the energy deposition from precipitating electrons,  $Q_p$ , which was computed following the method outlined by Wickwar *et al.* [1975], the electron temperature measured at 250 km and the ion temperature from 110 km of altitude. Figure 10d, reproduced from Figure 7j, displays the Poynting flux. The horizontal scale was changed using a constant arc motion of  $180 \text{ m s}^{-1}$ . Figure 10f shows the Joule heating rate, which was calculated according to the relation:  $JH \sim \Sigma_p(E + U \times B)^2$ . Figure 10g presents the height-integrated ion cooling rate due to collisions with the neutrals. Banks and Kockarts [1973] showed that the energy transfer rate

from ions to neutrals can be approximated as  $dU_i/dt = -n_i N_n \beta_{in} (T_i - T_n)$ , where  $N_n(N_i)$  and  $T_n(T_i)$  are the neutral (ion) density and temperature, and  $\beta_{in}$  is the ion energy loss rate.  $N_n$  and  $T_n$  were calculated using the MSIS-86 thermospheric model and an exospheric temperature equal to 850 K. The upper and lower traces correspond to the energy transferred to  $N_2$  particles (the major neutral constituent at E region altitudes) from  $N_2^+$  and  $O_2^+$  ions.

Figures 10a–10c show a prominent maximum occurring at 0211 UT. The coincidence of elevated temperature and enhanced  $\Sigma_p$  indicates the intrinsic relationship between these parameters. The second peak in  $T_e$  may be produced by the decrease in the electron cooling rate due to smaller values of  $N_e$ . Figures 10d–10g present a well-defined peak at 0220. In spite of the fact that some of these curves are not completely independent (the circulation of some of them includes common input parameters), the similarity in their shapes and location of their maxima suggests a direct relation.

A more quantitative view of the  $T_e$  and  $T_i$  enhancements associated with the center and dawnside of the February 26 arc is presented in Figure 11. The four profiles, labeled E or I, were obtained during the overhead transit of the arc, when the antenna was pointing antiparallel to **B**. The dashed lines

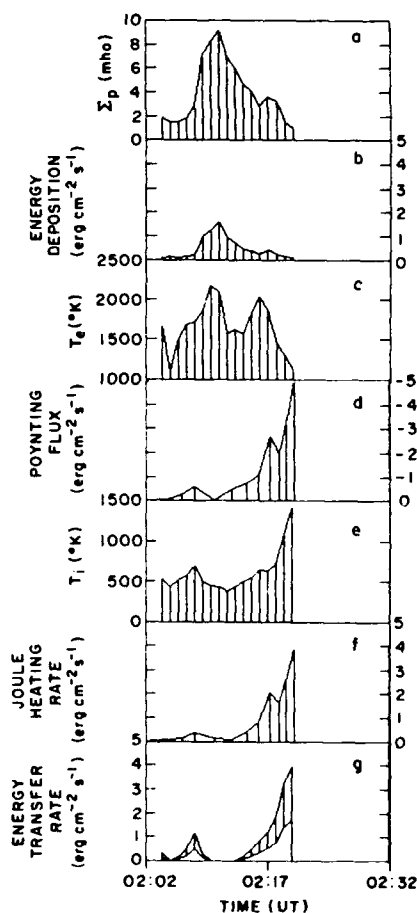


Fig. 10. Directly measured and derived parameters of the Sun-aligned arc of February 26, 1987: (a) height-integrated Pedersen conductivity; (b) energy deposition from precipitating electrons; (c)  $T_e$  at 250 km altitude; (d) Poynting flux; (e)  $T_i$  at 110 km; (f) Joule heating rate; and (g) energy transferred from ions to neutrals.



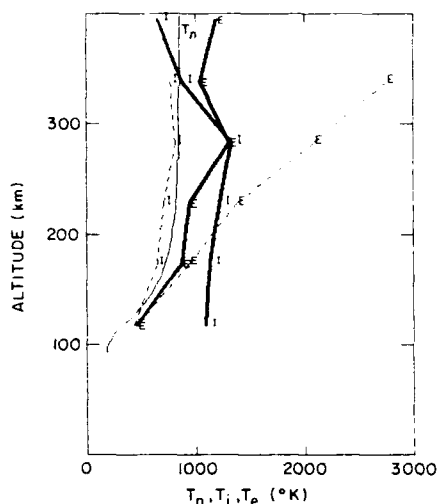


Fig. 11. Electron and ion temperatures measured during the up *B* position. Dashed lines correspond to 0211 UT and the thick solid line to measurements at 0220 UT. The thin trace represents the neutral temperature calculated using the MSIS-86 model.

are the electron (*E*) and ion (*I*) temperature profiles measured between 0211 and 0212 and when the region of higher density was being probed. The thick continuous traces are the  $T_e$  and  $T_i$  profiles measured at 0220 and near the dawnward edge of the arc. The  $T_e$  curve corresponding to the center of the Sun-aligned arc shows an enhancement of  $>1000$  K in the *F* region. Notice that this profile increases linearly at altitudes above 150 km. The  $T_i$  curve measured in the dawnside was enhanced by 700 K in the *E* and lower *F* regions.

#### 3.4. Thermal Analysis of the March 1, 1987 Elevation Scan

The isodensity contours on Figure 4c are reproduced in Plate 2. Superimposed on the  $N_e$  traces are two color-coded contours corresponding to the ion (blue) and electron (red) temperatures. The electron isothermal contour of 1000 K penetrates to lower altitudes near the regions of enhanced number density. The ion temperature is enhanced in the dawnside of the arc labeled A, reaching a value of 2000 K at 150 km. The duskside of arc B is also a region of high  $T_i$  values. This plot agrees and extends the observations shown in Figures 10 and 11.  $T_e$  and  $T_i$  are both enhanced but in different regions which do not necessarily collocate.  $T_e$  is enhanced at the dawn or dusk (or both) sides of the Sun-aligned arc.

Figure 12 has the same format as Figure 10. The curves shown in the seven panels were calculated based on the EL scan data of March 1, 1987. They correspond to arc A of Figure 4c. In spite of the large variability in the parameters displayed in this figure, the trend is the same: Regions of enhanced  $T_e$  are located near the center of the arc, and  $T_i$  enhancements are situated at the arc boundaries.

## 4. DISCUSSION

We have extensively analyzed two Sun-aligned arcs diagnosed by the incoherent scatter radar. Excepting unusual circumstances, this requires an ISR observing mode tailored

to nominal temporal and geometric properties of Sun-aligned arcs.

The two arcs studied here are relatively intense Sun-aligned arcs. This optimizes the statistical error bars on the parameters derived from the ISR data. One of the two arcs has been reported elsewhere [Niedzwiedzki *et al.*, 1989], with detailed analysis of its optical, ion production-loss rates, and ionizing flux properties. Observed in the UV by Polar Bear, and the visible from DMSP and ground-based imagers with time continuity, this is a well-documented example of a strong Sun-aligned arc. We show in Figure 3 that the position of its optical signature is colocated with the ISR signature. A second Sun-aligned arc is presented primarily to demonstrate that the key findings here are repeatable.

The observations reported here apply directly to Sun-aligned arcs bright enough to be readily seen by conventional all-sky cameras or visible and UV satellite images. The findings thus apply to stable Sun-aligned arcs as reported prior to the 1980s, which are found in the polar cap of the order of 5% of the time. The physical processes that we demonstrate are important in these arcs are, however, candidates for applying to a much broader class of arcs. The degree to which they represent the character of the much more common weaker Sun-aligned arcs [Weber and Buchau, 1981; Carlson *et al.*, 1988], found a third to a half of the time in the polar cap, is the subject of a separate study now in progress.

### 4.1. ISR Observing Mode

We have presented and illustrated an ISR mode which, we maintain, can in general identify and diagnose Sun-aligned arcs in the polar cap. Based on nominal properties of Sun-aligned arcs found with image-intensified all-sky photometers, the mode maps mesoscale (order  $10^3 \times 10^3$  km) areas with adequate time resolution to track the passage of arcs.

Arc identification is based on a two-step rationale. The ISR signature of the Sun-aligned arc is a Sun-aligned sheet or cylinder of persistent enhanced ionization below 200 km (at "*F*<sub>1</sub> region" or "photochemical" altitudes). For ionization to persist much below 200 km, it must represent the presence of ongoing ionization, because its chemical lifetime is so short. However, a region of stable or persistent production of Sun-aligned ionization must by the same token also be a region of stable or persistent Sun-aligned production of (electron impact excited) optical emissions. Thus when looking at contours of greater than  $10^5$  electrons  $\text{cm}^{-3}$  near 150 km, with chemical lifetime of order of a minute, and with persistence over 10 min, one cannot help but also expect to see enhanced airglow within the field-aligned projection of these contours. One example of this is shown in Figure 3.

### 4.2. Directly Observed Parameters

The directly observed parameters are electron density, electron and ion temperature, and plasma line-of-sight velocities. The electron densities show persistent Sun-aligned ridges of enhancements. Contours of constant electron density are Sun-aligned over mesoscale distances of 500–1000 km for altitudes between 100 and 200 km. Electron temperatures are enhanced along magnetic field lines above these enhanced ridges of ionization, consistent with the expecta-

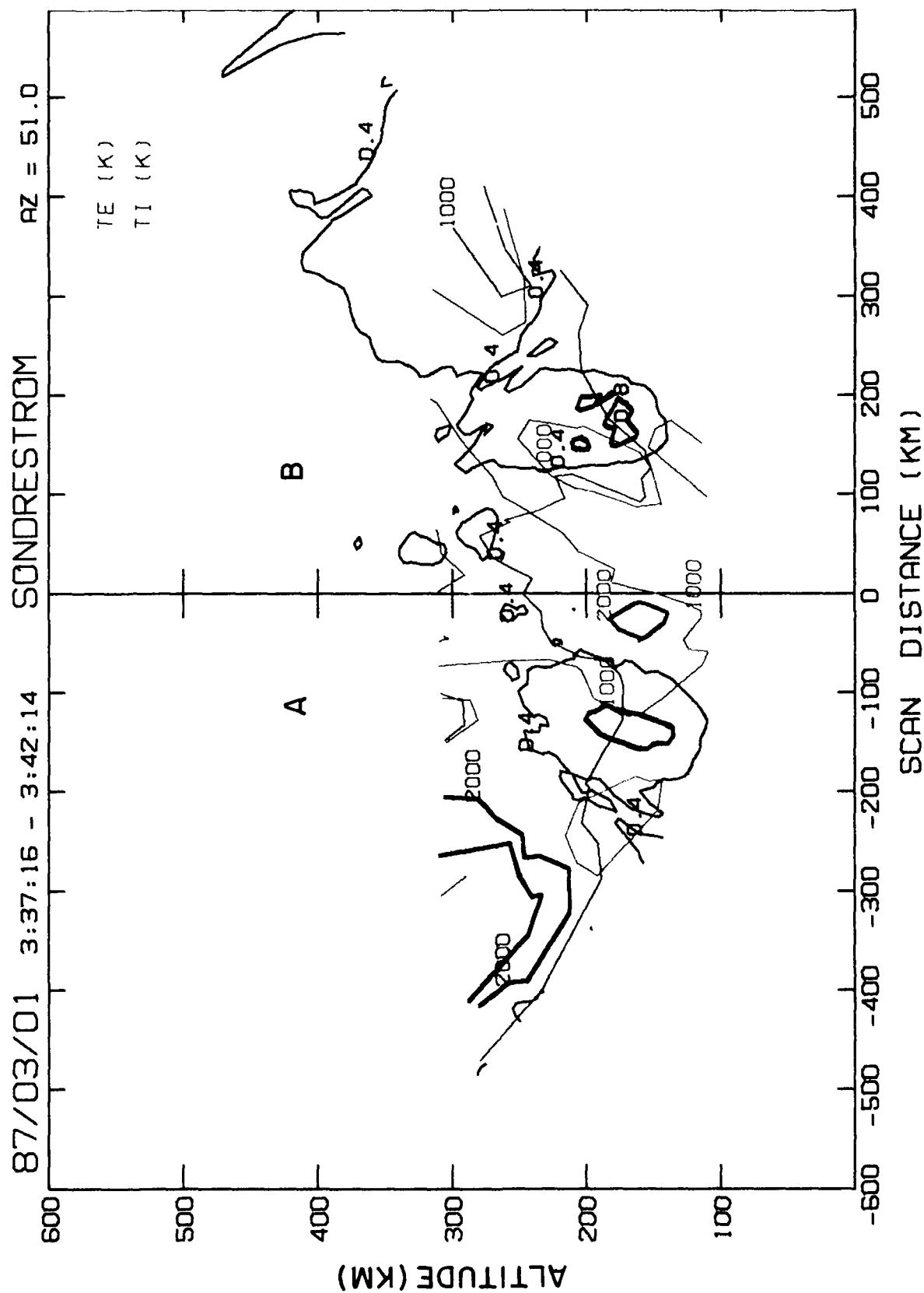


Plate 2. Superposition of the contours corresponding to three different parameters measured by the ISR: electron density (black),  $T_e$  (red) and  $T_i$  (blue). The data were taken on March 1, 1987 at 0337:16 UT.

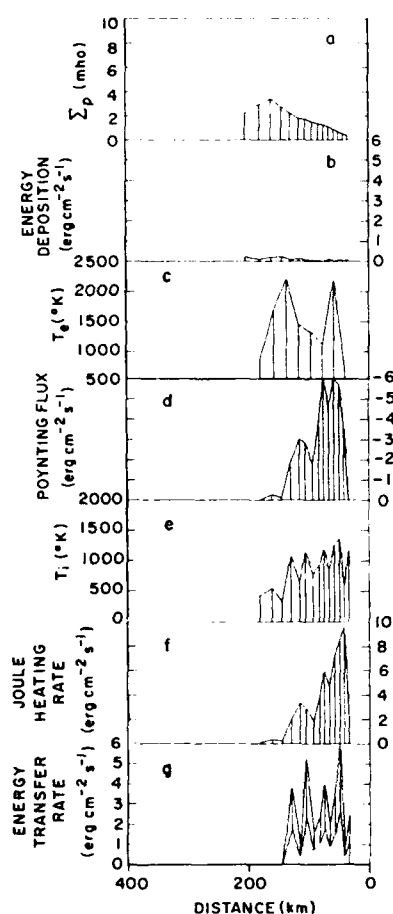


Fig. 12. Parameters derived from the left-hand half of the EL scan of 0337 UT on March 1, 1987. Figures 12a–12g display the same geophysical quantities as in Figure 10. The statistical uncertainties of  $T_e$  and  $T_i$  are 250 K and 500 K respectively.

tion of heating by a (sheet) flux of incident energetic electrons.

On the dawnside of the Sun-aligned arc, there is a channel of high ion temperature, exceeding that of the electron gas. This channel of ion heating is where the antisunward plasma flow is still near its maximum value. As one moves, dawn to dusk, into the arc, the ion temperature falls to equilibrium with the neutral particle gas, and only the electron gas has significantly enhanced temperature. These data confirm, refine, and extend the ion temperature enhancement finding and semiquantitative interpretation by Carlson *et al.* [1984]. Antisunward velocity gradients are both coaligned with the Sun-aligned contours of enhanced (below 200 km altitude) electron density. That is, where the antisunward plasma flow velocity decreases in going from dawn toward dusk, ionization is enhanced; when the dawn-to-dusk plasma velocity gradient has the opposite sense (increases dawn to dusk) or is constant, there is no enhanced ionization below 200 km. These confirm a simple arc electrodynamics interpretation (convergent electric fields produce converging Pedersen currents whose continuity is maintained across the arc by incident energetic electrons).

#### 4.3. Derived Parameters

The derived parameters are horizontal and Birkeland currents,  $E$  field, and Poynting and particle flux. We esti-

mated the steady state currents within the arc from the plasma density and velocity data. The Birkeland currents were calculated by two independent means. First the electron density contours of a cross section of the arc (found to match the density contours several hundred kilometers upstream and downstream and on earlier and later measurements) were used to estimate the steady state production rate of the arc, and hence the upward current above the arc carried by the estimated incident energetic electron flux. In the second method the horizontal electric field gradient across the arc was derived from the plasma velocity gradient across the arc. This electric field, applied to the ionospheric conductivity (derived from observed electron density profiles and a standard model atmosphere), led to derived Pedersen and Hall currents. Based on arc symmetry upstream and downstream, transarc gradients in calculated Pedersen currents were then used to derive (from the horizontal divergence of currents across the arc) the variation of Birkeland currents across the arc. The upward Birkeland currents derived from these two different approaches were comparable, and both peaked near the center of the arc at about  $1 \mu A m^{-2}$ . Because downward Birkeland currents (presumably carried by upgoing thermal electrons) can be derived only where electron densities are large enough to give a useful ISR signal, complete current mapping cannot be done. However, this approach gave a rather comprehensive estimate of the ionospheric current system in and near the stable Sun-aligned arcs observed, an estimate that should extrapolate well to such arcs in general. This is summarized in Figure 14.

We have performed three independent calculations of the energy into the Sun-aligned arc by nonparticle heating. While this nonparticle energy input is distributed across the full arc, it is strongest into the dawn edge. The three calculations are motivated by recognition that energy external to the ionosphere (ultimately mechanical energy in the solar wind) is carried down into the ionosphere along magnetic field lines as electromagnetic energy or Poynting flux. This is dissipated as frictional heating of the ions dragged through the neutral atmosphere, or Joule heating. Heat, initially deposited mostly in the ion gas, is rapidly passed onto the neutral gas.

The first calculation follows the rationale of a  $\delta E \times \delta B$  Poynting flux calculation. We note that the Sun-aligned arc changes much more slowly along than across its axis, and is very stable over times large compared to an Alfvén bounce period. Neglecting the spatial and time derivatives then, we take a cross section transverse to the arc, and slice it into a series of adjacent differential elements. We look at the electric field differential (dawn to dusk reduction) and Pedersen current differential across each element (the electric field is in this measured neutral wind rest frame). The current is then crossed against the electric field strength to derive the first estimate of energy, plotted in Figures 7j, 10d, and 12d, and labeled Poynting flux. Relative to an idealized measurement of Poynting flux this calculation has its shortcomings. Yet we feel it is useful, partly to underscore the real energy source, and partly because of the good quantitative agreement between the  $ergs cm^{-2} s^{-1}$  found from this calculation and from the following two.

The second calculation is based on the additional measurement of the ion gas temperature. Given the measured value of the plasma velocity and the neutral atmospheric velocity,

we can calculate the rate at which heat should be going into the ion gas, due to the relative motion of the ions through the neutral gas. This leads to the second estimate of energy flow, and is verified by the good agreement between the calculated and the actually observed ion temperature.

The third calculation deals with the heat loss from the ion gas, to the neutrals. It is based on the measured ion gas temperature and the neutral gas temperature. Because of the cooling rate cross section dependence on ion composition, which we do not measure, we show two values for the extremes of 100%  $\text{NO}^+$  versus 100%  $\text{O}_2^+$ . Within this relatively large uncertainty, this third energy estimate agrees with the first two (with better agreement for the more likely dominant ion).

We then applied an approximate energy balance calculation to these data. It was reasoned not only that was it logical to expect a magnetospheric energy source to drive the high-speed ionospheric plasma flow through thermospheric frictional-drag "loading," but that this energy dissipation should ultimately end up mostly in the neutral atmosphere below the enhanced ionospheric densities in the arc. It was possible to estimate this latter quantity in two ways: (1) from the steady state rate of heat going into the ion gas; and (2) from the steady state rate of heat lost from the ion gas. The former is derived from the conversion of ordered ion gas energy due to coherent motion under the action of the driving electric field, to disordered energy (heat) as the ions suffer randomizing collisions with neutral particles. This is proportional to the square of the difference between the ion and the neutral gas bulk velocity [Stubbe and Chandra, 1971]. The latter is derived from the observed difference between the neutral atmospheric and ion gas temperatures. Uncertainty in the ion composition leads to greater uncertainty in this latter estimate than in the former. However, both of these methods give a value for the energy deposition rate into the neutral atmosphere of a few  $\text{ergs cm}^{-2} \text{ s}^{-1}$ , comparable to the Poynting flux into this region. These three independent calculations thus lead to a simple but reassuringly self-consistent interpretation of the data.

It is important to note a critical step in the above argument before proceeding. We note that  $T_i$  can be derived in two complementary independent ways, one (theoretically) from measured ion and neutral particle velocities, the other directly from the radar-observed spectra. Our calculations of the differential temperature based on the ion and neutral velocities show good agreement with the observed  $T_i$  enhancements (see Plate 1a and Figure 7i). The Fabry-Perot also measured enhanced neutral temperatures, possibly collocated with the region of larger ion temperatures (R. Niciejewski, personal communication, 1989). The observed ion heating can be explained solely on the basis of a quantitative analysis of the large observed plasma flow  $\mathbf{V}$  relative to the observed neutral atmospheric rest frame  $\mathbf{U}$ . Since all three of these parameters are observed, not modeled, we are thus able to determine, not merely assume, that these ion temperatures are explained solely on the basis of this heating mechanism (within small statistical uncertainty). It is this use of the directly observed  $T_i$ ,  $\mathbf{V}$ , and  $\mathbf{U}$  that allows us to justify calculating the rate of heat flowing into the thermosphere on the basis of a steady state ion thermal balance argument.

We then point out that the magnitude of this heating rate is also of significance. The Poynting flux and energetic particle

flux deposit energy to the neutral atmosphere near and above 120 km of several  $\text{ergs cm}^{-2} \text{ s}^{-1}$  over the Sun-aligned arc of width of order 100 km. This compares to about  $0.5 \text{ erg cm}^{-2} \text{ s}^{-1}$  for a global mean thermospheric EUV heating rate. Parts of the arc experienced 10 times this reference average, and the average across the arc was three or four times this reference. Given that the arc is of order 100 km wide and persists for a few hours, it is a significant local heat source. It is not a negligible heat source even when averaged over its motion across the dark polar cap (of order 10% to tens of percent of the global mean EUV and thus comparable to a presently missing polar thermospheric heating component [e.g., Carlson and Crowley, 1989].) While the February 26 arc discussed is unusually intense, the polar cap under northward IMF conditions typically has several stable Sun-aligned arcs of a tenth or more of this visual (particle precipitation) intensity over a 2000 km or less polar cap width, with temporal persistence of order an hour or more. Estimates based on measured particle precipitation energy flux alone under these conditions may underestimate the thermospheric heating rate due to stable Sun-aligned arcs by a factor of 3 or more.

Note that for the March 1 Sun-aligned arc the particle precipitation energy (Figure 12) is about a sixth that for the February 26 case (Figure 10) although both arcs have comparable incident Poynting flux.

Here we have stressed taking advantage of the stability of the arc, in time and in space along its axial (Earth-Sun) dimension, to optimally diagnose its character. Ultimately, temporal and spatial variations must occur and become large enough to be of interest during one series of arc observations. During the 40 min observation of the February 26, 1987 arc, it drifted from overhead (0212 UT) to 100 km west (0225) to 180 km west (0234). A composite image of the arc was constructed from the many conical and planar cross sections of the arc to estimate departures from idealized constancy along its axial length. This analysis indicates a velocity gradient along the arc axis, with penetration of sunward drifting plasma only part way into the polar cap. The two-dimensional cross section (Figure 9) suggests flow from where the arc connects to the auroral oval, partial entry into the polar cap, and then clockwise rotational flow back to antisunward, exiting again from the polar cap. Farther into the polar cap there is slowing of antisunward plasma flow, but not a reversal to sunward. This is sketched schematically in Figure 13. (This is very reminiscent of the interpretation of some DE data by Hoffman *et al.* [1985] under similar conditions.)

It is clear from Figure 13 that the net velocity difference from the dawnside to the duskside of the arc is greater in the velocity reversal region than the merely velocity reduction region. Thus it is apparent from examination of this figure that the Pedersen current divergence, and balancing Birkebaek currents, lead to extra energetic particle input within the tongue of sunward moving plasma, relative to that in the region of simply a velocity gradient deeper in the polar cap. Furthermore, while Hall currents along the dawn edge of an arc of constant properties along its axial length simply continue into the polar cap, those in the region of partial penetration of sunward flow penetrate only partially into the polar cap and then must rotate westward near their region of maximum poleward penetration. These effects can combine to produce the "bright spot" or extra particle precipitation

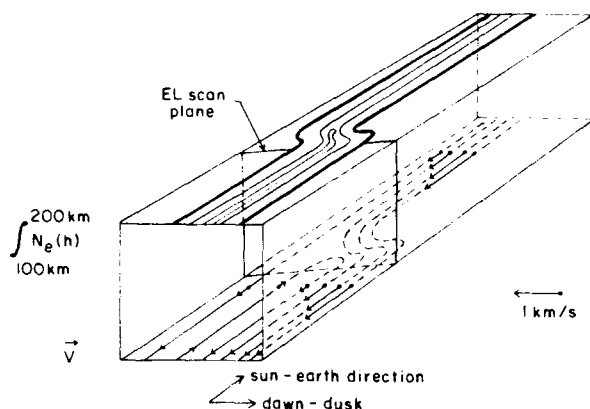


Fig. 13. Schematic representation of the height-integrated density (upper side) and the plasma flow pattern (lower surface). This figure is based on the EL and AZ scans of February 26, 1987.

often seen near where the Sun-aligned arc connects to the nightside auroral oval.

Finally, we condense the essential character we have found as characteristic of the electrodynamic, thermal, and energetic properties of these Sun-aligned arcs into the illustration of Figure 14. The character of these two sample arcs (February 26 near midnight MLT and March 1 post-midnight MLT, 1987), understood within the context of Figure 14, extends and extrapolates to at least the broad class of strong Sun-aligned arcs. We are now combining ISR and ASIP data for a large number of stable Sun-aligned arcs, to establish the extent to which these findings characterize typical polar cap conditions for northward IMF conditions [Carlson *et al.*, 1988].

The qualitative features of this "cartoon" must apply to

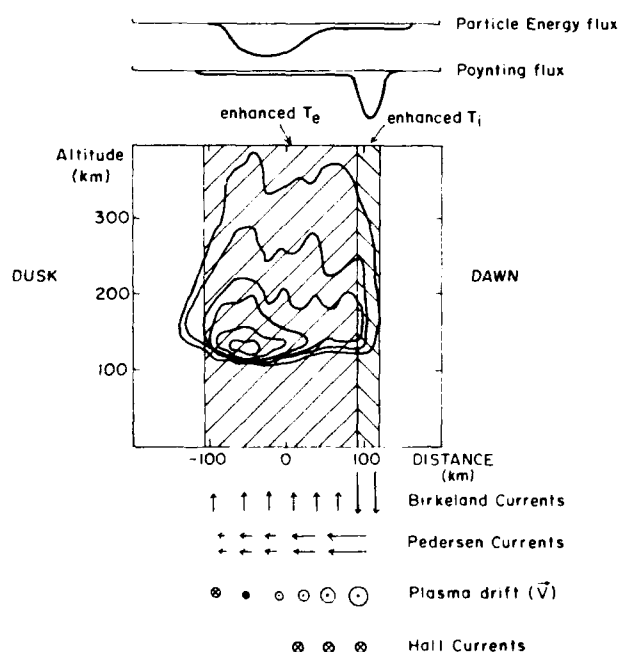


Fig. 14. Cross-sectional view of the Sun-aligned arc of February 26, 1987. Electrical parameters of the arc and energy going into the ionosphere are also indicated. This representation is in a semiquantitative fashion.

Sun-aligned arcs in general. Within the center of the arc, where  $N_e$  is enhanced below 200 km,  $T_e$  must be enhanced by the incoming flux of impact ionizing electrons. These must also carry an incoming particle energy flux, and an outgoing Birkeland current, to one side, while there must be a return (incoming) current on the other side. The Pedersen currents must decrease from dawn to dusk, as the antisunward plasma drifts must decrease from dawn to dusk. The plasma drifts may simply decrease, or reverse as in this illustration. The ion temperature will be enhanced where the difference between the plasma and neutral atmospheric velocities is sufficiently great. This depends on the thermospheric winds across the polar cap, and the extent to which plasma drifts may have strong sunward flow on the duskside of the arc.  $T_i$  will generally be enhanced on the dawnside, and occasionally on the duskside. Likewise, the Poynting flux typically peaks on the dawnside, but peaks on the duskside if there are strong sunward flows on the duskside. The magnitude of the Poynting flux is many  $\text{ergs cm}^{-2} \text{s}^{-1}$  for relatively intense Sun-aligned arcs, exceeding the particle energy, and smaller by a factor to be statistically defined for more common weaker arcs.

## 5. CONCLUSIONS

This study has led to the following.

1. The first direct measurement over full mesoscale horizontal areas (of order  $10^3 \times 10^3$  km) of persistent plasma velocity gradient across long-lived ( $\geq 10^3$  seconds) stable Sun-aligned arcs has been made. The sign of these gradients confirms simple arc electrodynamics. This is true for single and double Sun-aligned arcs observed.

2. New experimental diagnostic techniques have been developed, including illustration of an ISR observing mode capable of diagnosing polar electrodynamic features with temporal stability of at least several minutes and spatial coherence of at least 100 to a few hundred kilometers; extension of a potential fitting procedure to map polar plasma flow from ISR data; and illustration of a plasma rotational feature near where a Sun-aligned arc merges with the midnight auroral oval.

3. The cross sectional area map of the plasma density and thermal character across stable Sun-aligned arcs has been measured. The electron gas temperature is enhanced over the arc, supporting the expectation that the arc is produced by a sheet of incoming energetic electrons.

4. It has been determined that along the high-velocity dawnside of the incoming energetic electron sheet (producing the arc) there is a channel of enhanced ion temperature within which the ion temperature exceeds that of the electron gas. This Sun-aligned channel within which heat flows from the ion gas to the electron gas coincides with the high antisunward velocity channel along the dawn edge of the Sun-aligned region of enhanced electron density. In addition, if there is also return sunward flow at sufficiently high speed, ion heating is also found on the duskside of the arc. The ion gas heating can be explained solely on the basis of ion frictional drag of high plasma velocity in the thermosphere rest frame.

5. Persistent strong Joule heating driven by Poynting flux down into a Sun-aligned arc has been calculated and found to be at a rate well exceeding the particle energy flux. This rate is estimated by three independent calculations based on a

horizontal current differential, a velocity differential, and a temperature differential. Furthermore, the magnitude of this newly measured heat flux is several  $\text{ergs cm}^{-2} \text{s}^{-1}$  and as such is of significance to the polar thermospheric energy budget, and contributed to solution of the missing polar thermospheric heat source.

6. Present knowledge of the basic character of stable Sun-aligned arcs in the polar cap ionosphere has been extended to a relatively complete yet simple description, consistent with theoretical interpretation.

#### APPENDIX A

We show in this appendix that the LOS ion velocity measured by an ISR during elevation scans can be used to derive the full velocity vector ( $\mathbf{V}$ ). The only conditions for the determination of  $\mathbf{V}$  are that the LOS velocity from both  $E$  and  $F$  layers needs to be measured almost simultaneously, and the probed volumes need to be connected by the same magnetic line.

In the  $F$  region the ion motion is controlled by

$$\mathbf{V} = \mathbf{E} \times \mathbf{B}/B^2 \quad (\text{A1})$$

and for the  $E$  region

$$\mathbf{V} = (1 - k_2)\mathbf{U}_\perp + k_1\mathbf{U}_\perp \times \mathbf{B}/B + k_1\mathbf{E}/B + k_2\mathbf{E} \times \mathbf{B}/B^2 \quad (\text{A2})$$

where  $\mathbf{E}$ ,  $\mathbf{V}$ , and  $\mathbf{U}_\perp$  are the electric field, the ion velocity and the neutral wind in a plane perpendicular to  $\mathbf{B}$ . With

$$k_1 = \frac{\nu_i \Omega_i}{\nu_i^2 + \Omega_i^2} \quad (\text{A3})$$

$$k_2 = \frac{\Omega_i^2}{\nu_i^2 + \Omega_i^2} \quad (\text{A4})$$

$\nu_i$  is the ion-neutral collision frequency and  $\Omega_i$  the ion gyrofrequency. The line of sight velocity ( $V_{\text{LOS}}$ ) depends on the velocity vector according to

$$V_{\text{LOS}} = \mathbf{V} \cdot \mathbf{A} \quad (\text{A5})$$

where  $\mathbf{A}$  is the unit vector in the antenna pointing direction expressed in magnetic coordinates.

The transmitted pulse pattern consisted of two pulses, a narrow pulse,  $30 \mu\text{s}$  (4.5 km) long, and a long pulse,  $320 \mu\text{s}$  (48 km) in length. Data sampling time was set equal to  $8 \mu\text{s}$  and a 32-lag autocorrelator was used to provide the ac function of the incoherent scatter signal. This setup allows the spectra to accept contributions from a range of 82 km. The volume probed by the single long pulse during one integration period is equal to the product of 82 km, the arc segment scanned during the integration time and the radar beam width. In the  $E$  region, the number density, the ion velocity and the neutral wind vary with altitude very rapidly; in this sense the long pulse measurements are not able to resolve narrow layers and only provide a weighted average over the entire  $E$  region. This weighting factor depends on the local number density the inverse of the range squared and a triangular function to compensate for the fact that all the lag products have different spatial resolution which linearly decrease for the longer delays. Expressions (A1) and (A2) were weighted following the procedure described before, then multiplied by the  $\mathbf{A}$  vectors to form dot products

for the  $E$  and  $F$  layers [Brekke *et al.*, 1973] and made equal to the measured LOS velocities.

Radar observations are subject to several types of constraints which need to be considered in any calculation of the velocity vectors. One of them is related to the drift of the S-A arcs. These arcs move along the dawn-dusk meridian, and the Earth rotational motion will modulate the measured velocities resulting in the following distortions. (1) The Doppler velocity is reduced by the term  $\mathbf{V}_c \cdot \mathbf{A}$ , where  $\mathbf{V}_c$  is the corotation velocity. At Sondrestrom  $\mathbf{V}_c$  is equal to  $180 \text{ m s}^{-1}$ . (2) There is also a small spatial displacement between contiguous integration periods, equal to  $(\mathbf{V}_c + \mathbf{V}_{\text{arc}}) \times T$ , where  $\mathbf{V}_{\text{arc}}$  is the velocity of the arc with respect to a fixed frame, and  $T$  is the time interval between  $E$  and  $F$  region measurements (about 30 s). Although this effect is small (6 km), it could generate significant errors when the  $E$  region measurements are mapped to the  $F$  region. The large range resolution (82 km) hinders also the ability to resolve the vector. In particular, low-elevation measurements can include a large contribution of the horizontal variations of the ion flow (i.e., plasma boundaries).

In a strict sense the  $E$  to  $F$  region mapping algorithm can be employed only for data that have been collected in a plane coincident with the  $\mathbf{B}$  field; for Sondrestrom, this corresponds to  $-39^\circ$  azimuth. During our experiments the EL scans were performed at  $-129^\circ$  and  $51^\circ$  azimuth; consequently, the  $E$  region projections of the  $F$  region measurements are located slightly north and west of the measured  $E$  layer values. However, for the data presented here, the arcs were aligned  $-24^\circ$  and  $-25^\circ$  with respect to geographic north, and the equipotential contours (aligned with the arc) deviate  $14^\circ$  or  $15^\circ$  from the magnetic meridian. The  $E$  region intersections were between 1 or 2 km away from equipotential lines that crossed the  $E$  region measurements.

In order to gain some confidence in the analysis of data from EL scans, we performed a zero order calculation of the velocity vector using the LOS velocities measured at 110 and 160 km of altitude and 105 km of distance (see arrow in Figure 2e). For simplicity  $\mathbf{U}_\perp$  is considered to be zero and  $\mathbf{B}$  to be pointing downward. After subtracting the corotation term the radar LOS velocities are  $V_{\text{LOS}}(E) = 173 \text{ m s}^{-1}$ ,  $V_{\text{LOS}}(F) = -101 \text{ m s}^{-1}$ . Equations (A1) and (A5) indicate that the velocity component along the scan is  $-168 \text{ m s}^{-1}$ . Then, using (2),  $k_1 = 0.292$  and  $k_2 = 0.298$ ; the other component (perpendicular to the scan) is  $-968 \text{ m s}^{-1}$ . After a rotation to geographic coordinates, we obtain  $V_{\text{east}} = 739 \text{ m s}^{-1}$  and  $V_{\text{south}} = 647 \text{ m s}^{-1}$ . Instead, when we use all the terms of (A2), the IGRF-85 model of  $\mathbf{B}$ , a second  $V_{\text{LOS}}$  measurement in the  $F$  region and the neutral wind from the Fabry-Perot, the result is  $V_{\text{east}} = 647$ ,  $V_{\text{south}} = 900 \text{ m s}^{-1}$ . This is a velocity that points closer to the antisunward direction. All the derived velocities ( $\mathbf{V}$ ) presented in Figures 4-8 were obtained using the more precise and complete algorithm that considered all the terms of (A1)-(A5). The zero approximation shown above can be employed when a computer is not available.

#### APPENDIX B

The LOS velocity measured during radar azimuthal scans can also be used to derive the ionospheric electric field  $\mathbf{E}$ , on the velocity vector, using the property of  $\mathbf{E}$  of being irrotational. The electric field is derivable from a scalar potential following

$$\mathbf{E} = -\nabla V \quad (\text{B1})$$

where  $V$  is the electrostatic potential that varies as a function of latitude and longitude. Now, if the scan is performed at a low elevation, then  $V$  can be represented by  $V(r, a)$ , where  $r$  is range and  $a$  the azimuth.

An incoherent backscatter radar measures the radial component of the ion velocity at several distances along the line of sight. At high latitudes this radial drift is closely related to the azimuthal component of  $\mathbf{E}$ . Consequently,  $V$  could be determined by integrating the azimuthal component of (B1) and using a known initial value of the potential,  $V(r, a_0)$ . At the Millstone Hill radar, the boundary potential can be assumed to be null at the southernmost part of the scan [Holt *et al.*, 1984]. However, no similar statement can be used to reduce data from Sondrestrom.

Another method that has been used to resolve the magnitude and the direction of the ion flow is the beam swinging technique. Here, the LOS velocity from several adjacent azimuthal sectors are least squared fitted to extract the three components of the velocity [Hagfors and Behnke, 1974]. This method has been employed at Arecibo, where the more uniform ionosphere of this mid-latitude station grants confidence for the application of this type of analysis.

Although  $V(r, a_0)$  could be calculated from the velocity vectors of section 3.1, we instead computed the boundary potential using the data from the same azimuthal scan. We employed the LOS velocity of three adjacent integration periods and the condition of negligible ion motion along  $B$  (less than or of order  $25 \text{ m s}^{-1}$  as measured) to obtain space-averaged velocity vectors. Then, the initial boundary potential was calculated for every integration period and served as the initial condition for the more precise value of  $V$  which was obtained by integrating (B1). The boundary potential as calculated in this way smooths rapid spatial variations of the velocity but will be less affected by statistical errors. This scheme was adopted to avoid cumulative errors produced by random fluctuations in  $V_{\text{LOS}}$  which sometimes are of the same order of magnitude as the measured velocity.

**Acknowledgments.** We would like to acknowledge S. Basu and Su. Basu for critical readings of the manuscript, R. Niciejewski and J. Meriwether for useful conversations concerning the FPI data, E. Weber for providing the ASIP image data, and J. Kelly for making the radar data available for this study. This research was supported in part by Air Force Office of Scientific Research under task 2310G9. The work at Boston College was supported by Geophysics Laboratory F19628-90-K-0007. We thank the Danish Commission for Scientific Research in Greenland for permission to conduct these experiments.

The Editor thanks two referees for their assistance on this paper.

## REFERENCES

- Akasofu, S.-I., Recent progress in studies of DMSP auroral photographs, *Space Sci. Rev.*, **19**, 169, 1976.
- Akasofu, S.-I., R. Williams, and M. Roederer, Effects of the passage of an IMF discontinuity on the polar cap geometry and the formation of a polar cap arc, *Planet. Space Sci.*, **32**, 119, 1984.
- Banks, P. M., and G. Kockarts, *Aeronomy: Part B*, Academic, San Diego, Calif., 1973.
- Baron, M. J., and R. H. Wand,  $F$  region ion temperature enhancements resulting from Joule heating, *J. Geophys. Res.*, **88**, 4114, 1983.
- Berkey, T., L. L. Cogger, S. Ismail, and Y. Kamide, Evidence for a correlation between Sun-aligned arcs and the interplanetary magnetic field direction, *Geophys. Res. Lett.*, **3**, 145, 1976.
- Brekke, A., J. R. Doupnik, and P. M. Banks, A preliminary study of the neutral wind in the auroral  $E$  region, *J. Geophys. Res.*, **78**, 8235, 1973.
- Brekke, A., J. R. Doupnik, and P. M. Banks, Incoherent scatter measurements of  $E$  region conductivities and currents in the auroral zone, *J. Geophys. Res.*, **79**, 3773, 1974.
- Burke, W. J., M. C. Kelley, R. C. Sagalyn, and M. Smiddy, and S. T. Lai, Polar cap electric field structures with a northward interplanetary magnetic field, *Geophys. Res. Lett.*, **6**, 21, 1979.
- Burke, W. J., M. S. Gussenhoven, M. C. Kelley, D. A. Hardy, and F. J. Rich, Electric and magnetic field characteristics of discrete arcs in the polar cap, *J. Geophys. Res.*, **87**, 2431, 1982.
- Carlson, H. C., Jr., and G. Crowley, The equinox transition study: An overview, *J. Geophys. Res.*, **94**, 16,861, 1989.
- Carlson, H. C., V. B. Wickwar, E. J. Weber, J. Buchau, J. G. Moore, and W. Whiting, Plasma characteristics of polar cap  $F$ -layer arcs, *Geophys. Res. Lett.*, **11**, 895, 1984.
- Carlson, H. C., R. A. Heelis, E. J. Weber, and J. R. Sharber, Coherent mesoscale convection patterns during northward interplanetary magnetic field, *J. Geophys. Res.*, **93**, 14,501, 1988.
- Davis, T. N., The morphology of the polar aurora, *J. Geophys. Res.*, **65**, 3497, 1960.
- de la Beaujardiere, O., R. R. Vondrak, and M. J. Baron, Radar observations of electric fields and currents associated with auroral arcs, *J. Geophys. Res.*, **82**, 5051, 1977.
- Denholm, J. V., and F. R. Bond, Orientation of polar auroras, *Aust. J. Phys.*, **14**, 193, 1961.
- Doupnik, J. R., A. Brekke, and P. M. Banks, Incoherent scatter radar observations during three sudden commencements and a Pc 5 event on August 4, 1972, *J. Geophys. Res.*, **82**, 499, 1977.
- Eather, R. H., and S.-I. Akasofu, Characteristics of polar cap auroras, *J. Geophys. Res.*, **74**, 4794, 1969.
- Fedder, J. A., and P. M. Banks, Convection electric fields and polar thermospheric winds, *J. Geophys. Res.*, **77**, 2328, 1972.
- Frank, L. A., J. D. Craven, J. L. Burch, and J. D. Winningham, Polar views of the Earth's aurora with Dynamic Explorer, *Geophys. Res. Lett.*, **9**, 1001, 1982.
- Frank, L. A., et al., The theta aurora, *J. Geophys. Res.*, **91**, 3177, 1986.
- Gussenhoven, M. S., Extremely high latitude auroras, *J. Geophys. Res.*, **87**, 2401, 1982.
- Hagfors, T., and R. A. Behnke, Measurement of the three-dimensional plasma velocities at the Arecibo Observatory, *Radio Sci.*, **9**, 89, 1974.
- Hardy, D. A., Intense fluxes of low-energy electrons at geomagnetic latitudes above  $85^\circ$ , *J. Geophys. Res.*, **89**, 3883, 1984.
- Hedin, A. E., MSIS-86 thermospheric model, *J. Geophys. Res.*, **92**, 4649, 1987.
- Hoffman, R. A., R. A. Heelis, and J. S. Prasad, A Sun-aligned arc observed by DMSP and AE-C, *J. Geophys. Res.*, **90**, 9697, 1985.
- Holt, J. M., R. H. Wand, and J. V. Evans, Millstone Hill measurements on 26 February 1979 during the solar eclipse and formation of a midday  $F$ -region trough, *J. Atmos. Terr. Phys.*, **46**, 251, 1984.
- Huang, C. Y., L. A. Frank, W. K. Peterson, D. J. Williams, W. Lennartsson, D. G. Mitchell, R. C. Elphic, and C. T. Russell, Filamentary structures in the magnetotail lobes, *J. Geophys. Res.*, **92**, 2349, 1987.
- Ismail, S., D. D. Wallis, and L. L. Cogger, Characteristics of polar cap Sun-aligned arcs, *J. Geophys. Res.*, **82**, 4741, 1977.
- Kan, J. R., and W. J. Burke, A theoretical model of polar cap auroral arcs, *J. Geophys. Res.*, **90**, 4171, 1985.
- Lassen, K., and C. Danielsen, Quiet time pattern of auroral arcs for different directions of the interplanetary magnetic field in the  $Y-Z$  plane, *J. Geophys. Res.*, **83**, 5277, 1978.
- Mende, S. B., J. H. Doolittle, R. M. Robinson, R. R. Vondrak, and F. J. Rich, Plasma drifts associated with a system of Sun-aligned arcs in the polar cap, *J. Geophys. Res.*, **93**, 256, 1988.
- Meng, C.-I., The auroral electron precipitation during extremely quiet geomagnetic conditions, *J. Geophys. Res.*, **86**, 4607, 1981.
- Meng, C.-I., and S.-I. Akasofu, The relation between the polar cap auroral arc and the auroral oval arc, *J. Geophys. Res.*, **81**, 4004, 1976.
- Murphree, J. S., C. D. Anger, and L. L. Cogger, The instantaneous relationship between polar cap and oval auroras at times of

- northward interplanetary magnetic field. *Can. J. Phys.*, **60**, 349, 1982.
- Niciejewski, R. J., et al., Coordinated satellite and ground-based measurements of the energy characteristics of a Sun-aligned arc over Sondre Stromfjord. *J. Geophys. Res.*, **94**, 17,201, 1989.
- Obara, T., M. Kitayama, T. Mukai, N. Kaya, J. S. Murphree, and L. L. Cogger, Simultaneous observations of Sun-aligned polar cap arcs in both hemispheres by EXOS-C and Viking. *Geophys. Res. Lett.*, **15**, 713, 1988.
- Peteherych, S., G. G. Shepherd, and J. K. Walker, Observations of vertical *E* region neutral winds in the intense auroral arcs. *Planet. Space Sci.*, **33**, 869, 1985.
- Peterson, W. K., and E. G. Shelley, Origin of the plasma in a cross-polar cap auroral feature (theta aurora). *J. Geophys. Res.*, **89**, 6729, 1984.
- Reiff, P. H., and J. L. Burch, IMF  $B_z$ -dependent dayside plasma flow and Birkeland currents in the dayside magnetosphere. 2. A global model for northward and southward IMF. *J. Geophys. Res.*, **90**, 1595, 1985.
- Robinson, R. M., R. R. Vondrak, and E. Friis-Christensen, Ionospheric currents associated with a Sun-aligned arc connected to the auroral oval. *Geophys. Res. Lett.*, **14**, 656, 1987.
- Romick, G. J., and N. B. Brown, Midday auroral observations in the oval, cusp region and polar cap. *J. Geophys. Res.*, **76**, 8420, 1971.
- Schunk, R. W., and J. C. G. Walker, Thermal diffusion in the  $F_2$  region of the ionosphere. *Planet. Space Sci.*, **18**, 535, 1970.
- Spencer, N. W., R. F. Theis, L. E. Wharton, and G. R. Carignan, Local vertical motions and kinetic temperature from AE-C as evidence for auroral-induced gravity waves. *Geophys. Res. Lett.*, **3**, 313, 1976.
- Stubbe, P., and S. Chandra, Ionospheric warming by neutral winds. *Planet. Space Sci.*, **19**, 731, 1971.
- Weber, E. J., and J. Buchau, Polar cap *F*-layer auroras. *Geophys. Res. Lett.*, **8**, 125, 1981.
- Weber, E. J., et al., Rocket measurements within a polar cap arc: Plasma, particle and electric circuit parameters. *J. Geophys. Res.*, **94**, 6692, 1989.
- Went, G., Aspects de l'aurore observée à la base Dumont-d'Urville en Terre Adélie. *C. R. Acad. Sci.*, **246**, 2925, 1958.
- Wickwar, V. B., M. J. Baron, and R. D. Sears, Auroral energy input from energetic electrons and Joule heating at Chatanika. *J. Geophys. Res.*, **80**, 4364, 1975.
- H. C. Carlson, Jr., Geophysics Laboratory, Hanscom Air Force Base, MA 01731.
- C. E. Valladares, Institute for Space Research, Boston College, Newton Center, MA 02159.

(Received October 27, 1989;  
revised August 6, 1990;  
accepted August 6, 1990.)